A conserved in-frame stop codon acts as a multipotent defense mechanism in alphaviruses

Tamanash Bhattacharya[1,*], Tiia S. Freeman[1], Eva M. Alleman[1†], Fang Wang[3], Lyuba Chechik[3], Michael Emerman[1,2], Kevin M. Myles[3], & Harmit S. Malik[1,4]

[1] Basic Sciences Division, Fred Hutchinson Cancer Center, Seattle, WA, USA

[2] Human Biology Division, Fred Hutchinson Cancer Center, Seattle, WA, USA

[3] Department of Entomology and AgriLife Research, Texas A&M University, College Station, TX, USA

[4] Howard Hughes Medical Institute, Fred Hutchinson Cancer Center, Seattle, WA, USA

[†] Present address: Molecular and Cellular Biology Program, University of Washington, Seattle, WA, USA

Abstract

Most alphaviruses maintain an in-frame opal stop codon that interrupts their non-structural polyprotein (nsP) ORF between nsP3 and nsP4 in both vertebrate and insect hosts. We show that the nsP3 opal stop codon confers a replicative advantage to Sindbis virus (SINV) in RNAi-competent mosquito cells and *Aedes albopictus* mosquitoes, but not in cells or mosquitoes lacking RNAi. Mutation of the opal stop codon delays processing of the viral nsP polyprotein, which disrupts viral replication spherule integrity, and renders viral RNA susceptible to Dicer 2-cleavage, resulting in higher antiviral siRNA responses against SINV. Similarly, these defects caused by opal codon mutations lead to increased detection of viral RNA and enhanced antiviral interferon signaling in vertebrate cells. Thus, a single stop codon in alphaviruses mediates a multipotent viral strategy to evade innate immune defenses in diverse hosts.

Teaser

A conserved ORF-interrupting stop codon helps alphaviral RNAs avoid triggering antiviral innate immunity in diverse hosts.

Introduction

Most alphaviruses encode an in-frame premature opal (UGA) stop codon within the non-structural polyprotein (nsP) open reading frame at the end of the *non-structural protein 3 (nsP3)* gene, just before the *non-structural protein 4 (nsP4)* gene (Figure 1A) (*1*). Programmed ribosomal readthrough (PRT) at this opal stop codon enables alphaviruses to produce two different polyproteins from their *nsP* genes: the standard translation produces the nsP1-nsP2-nsP3 polyprotein (P123), whereas PRT results in the longer nsP1-nsP2-nsP3-nsP4 polyprotein (P1234) (*2*). Sufficient levels of PRT are vital for viral replication, as nsP4 functions as the viral RNA polymerase required to generate new viral RNA (*3*).

There has been considerable interest in understanding how and why the opal codon provides a fitness advantage to alphaviruses (*4–7*). We recently demonstrated that the opal codon provides a fitness advantage to alphaviruses in vertebrate cells by resolving a temperature-dependent trade-off between nsP4 expression via PRT and the proteolytic processing efficiency of the viral nsP (*1*). We showed that the opal codon at nsP3 position 550 (550opal) is strongly preferred over non-opal (sense codon) substitutions at this site in vertebrate cells that grow at 37°C. Yet, why this opal codon is maintained in insect hosts remains unknown, since, in contrast to vertebrate cells at 37°C, non-opal substitutions are much better tolerated in vertebrate cells or in *Aedes albopictus*-derived C6/36 mosquito cells grown at 28°C (*1*, *7*, *8*). Moreover, previous studies with distinct alphaviruses, including SINV and Eastern equine encephalitis virus (EEEV), showed that Opal-to-Cysteine substitutions may even provide a replicative fitness advantage over the wild-

type opal codon in mosquito C6/36 cells (*1*, *9*). Despite this apparent fitness benefit, opal-to-sense codon substitutions are exceedingly rare (3%) in alphaviruses isolated from mosquitoes and are entirely absent in closely related insect-specific alphaviruses (Figure S1A-B) (*10–12*). Thus, additional host or environmental factors must contribute to the conservation of the nsP3 opal stop codon in insect hosts.

A key factor that could select for the opal codon to be preserved among alphaviruses is innate immunity in insect hosts. Alphaviruses elicit a robust small RNA response in mosquito cells, mediated primarily through the siRNA pathway (*13–15*). Following viral infection, Dicer 2 (Dcr2), a key mediator in the short interfering RNA (siRNA) pathway, processes viral double-stranded RNA (dsRNA) replication intermediates into 21-nt-long virus-derived small interfering RNAs (vsiRNAs). These vsiRNAs form a complex with Argonaute 2 (Ago2) and other components of the RNA-induced silencing complex (RISC) to target nascent single-stranded viral RNA for cleavage and degradation (*16*, *17*). However, most previous experimental passaging studies were conducted using C6/36 cells, which lack an effective antiviral RNA interference (RNAi) response due to impaired Dcr2 function (*18*).

Here, we investigated whether immune pressures from RNAi might explain the retention of the opal codon in insect hosts using the prototype alphavirus Sindbis virus (SINV) as our model. We found that an Opal-to-Cysteine substitution (SINV 550C) enables SINV to replicate better than wild-type SINV (550opal) in *Aedes albopictus*-derived RNAi-deficient C6/36 cells or in U4.4 cells depleted of key RNAi proteins. However, the SINV 550C variant is significantly less fit than wild-type SINV (550opal) in RNAi-competent U4.4 cells. We corroborate these findings *in vivo* using infections of either wild-type SINV (550opal) or SINV 550C viruses in wild-type or *Dcr2*-knockout *Aedes aegypti* mosquitoes. Using cytological assays, we demonstrate that the integrity of intracellular viral replication compartments (spherules) is compromised in SINV 550C infections but not in 550opal infections, due to delays in nsP processing. This lack of spherule integrity does not impair SINV 550C fitness in the absence of RNAi. However, in RNAi-competent mosquito cells, the lack of spherule integrity enables host antiviral defenses, such as Dcr2, to access viral dsRNA and induce a significantly higher antiviral siRNA response, thereby lowering the fitness of the SINV 550C variant. Thus, we conclude that alphaviruses retain the opal codon to protect against the RNAi immune response in insect hosts. We also demonstrate that SINV and other alphaviruses utilize structured RNA elements within their genomes to generate ‘decoy’ vsiRNAs, which blunt the mosquito RNAi response when spherule integrity is compromised. We further demonstrate that compromised spherule integrity also triggers increased viral RNA detection by cytoplasmic RNA sensors in vertebrate cells, leading to SINV 550C infections producing a more robust antiviral interferon response. Thus, by ensuring timely polyprotein processing, the opal codon helps maintain spherule integrity, limiting access to host cytoplasmic proteins that detect or cleave viral dsRNA in both insect and vertebrate hosts. Collectively, these findings suggest that alphaviruses maintain the opal stop codon as a defensive strategy in both insect and vertebrate hosts.

Results

The Dcr2-dependent siRNA pathway imposes selection against non-opal codon variants

The Dcr2-dependent siRNA pathway serves as the primary antiviral response against alphavirus infections in mosquitoes (*13*). *Aedes albopictus*-derived C6/36 cells lack functional Dicer 2 (Dcr2) due to a frameshift mutation within the *Dcr2* open reading frame, resulting in a Dcr2 protein that lacks the RNase III domains essential for dicing activity (*18*). To investigate whether Dcr2 deficiency explains the tolerance of opal codon substitution variants in C6/36 cells, we compared the growth of three opal-to-sense substitution variants (550Alanine, 550Arginine, 550Cysteine) in *Dcr2*-competent U4.4 cells or *Dcr2*-lacking C6/36 cells. To ensure quantifiable virus growth in RNAi-competent cells, all infections were performed at moderately high MOI (≥4). Consistent with our previous study (*1*), we found that the infection rates of the 550C and 550A variants were higher than those of wild-type SINV (550opal) in Dcr2-lacking C6/36 cells, whereas the SINV 550R variant was less fit. In contrast, infection rates of all sense-codon variants were significantly reduced in Dcr2-competent U4.4 cells compared to wild-type SINV (550opal) (Figure 1B).

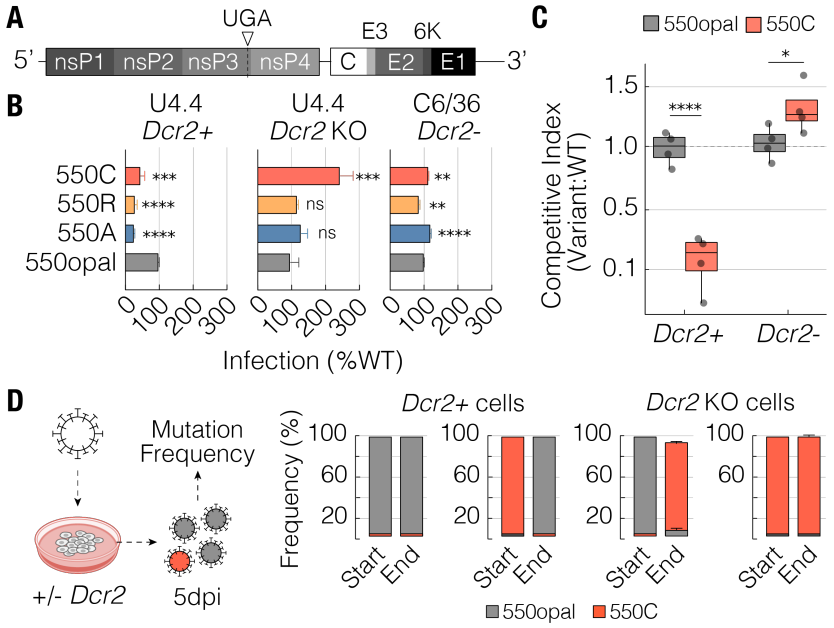

Figure 1. The mosquito RNAi pathway imposes strong selection on the alphavirus nsP3/4 opal codon. (A) Alphaviruses encode a premature in-frame opal codon within the non-structural open reading frame at the 3' end of the nsP3 gene. **(B)** Infection rates of opal-to-sense substitution SINV variants relative to wild-type SINV in Aedes albopictus cells: either U4.4 cells with functional Dcr2 (*Dcr2*+) or CRISPR/Cas9-edited Dcr2-deficient (*Dcr2 KO*) U4.4 cells, or (*Dcr2*-) C6/36 cells. Data represent the mean of at least three independent biological replicates. **(C)** Competitive fitness of SINV 550C variant against wild-type SINV 550opal in *Dcr2*+ U4.4 or *Dcr2*- C6/36 cells. Wild-type versus wild-type competition was performed as a control. The data represent four independent biological replicates. Error bars represent the standard error of the mean (SEM). Two-way ANOVA with Tukey's test for multiple comparisons. **** = $p < 0.0001$, *** = $p < 0.001$, ** = $p < 0.01$, * = $p < 0.05$, ns = not significant. **(D)** Wild-type SINV (with opal codons, UGA) or 550C SINV variants (with UGC/UGU codons) were passaged for 5 days in *Dcr2*+ U4.4 cells or CRISPR-edited U4.4 *Dcr2 KO* cells. The frequencies of opal versus cysteine codons at the start and end of the passaging, as determined via small RNA sequencing, are reported. The data represent three independent biological replicates.

Both U4.4 and C6/36 cells are derived from *Aedes albopictus*. Nevertheless, differences between these cell lines beyond their Dcr2 status could influence SINV infection. To compare the fitness of viral variants within isogenic host cell lines, we used CRISPR/Cas9 to create *Dcr2* knockout (*Dcr2 KO*) U4.4 cells, resulting in a heterogeneous cell population in which *Dcr2* was knocked out in ~82-85% of the cells (Figure S2). Despite the incomplete nature of this knockout, we found that infection rates of all SINV opal-to-sense variants, including SINV 550R, were comparable (550A, 550R) or higher (550C) than wild-type SINV (550opal) (Figure 1B). Thus, in both C6/36 and U4.4 cells, the loss of *Dcr2* enhances the fitness of SINV opal-to-sense variants.

Our recent comprehensive profiling of the SINV opal codon in *Dcr2*-deficient mosquito cells showed that cysteine is the most tolerated sense codon (*1*). Cysteine is also the only opal-to-sense substitution observed in SINV in nature (*19*). We therefore carried out all subsequent comparative analyses using wild-type SINV and SINV 550C, which represents an opal-to-sense mutation. Consistent with the independent growth assays, our competition experiments revealed that SINV 550C fitness is significantly lower than that of 550opal in *Dcr2*-competent U4.4 cells, but higher than that of wild-type SINV in *Dcr2*-lacking C6/36 cells (Figure 1C), recapitulating our previous findings (*1*).

We also evaluated the selective pressure imposed by intact Dcr2 by passaging SINV 550C variants across three independent replicate lineages during a five-day infection, *i.e.,* approximately 24 rounds of replication (Figure 1D). We found that SINV550C was almost entirely replaced by 550opal in *Dcr2*-competent U4.4 cells, implying that mutations reverting 550C to 550opal had occurred and swept through the population within just 24 rounds of replication. In contrast, we found that 550C variants were still maintained in U4.4 *Dcr2* KO cells (Figure 1D). Conversely, when we passaged 550opal variants in U4.4 *Dcr2* KO cells, we found that they almost completely converted to 550sense variants, primarily 550C (UGC or UGU codons), within 5 days. Yet, 550opal variants were still maintained upon passaging in *Dcr2*-competent U4.4 cells (Figure 1D). The rapid gain of opal-to-sense substitutions in *Dcr2* KO U4.4 cells mirrors prior findings in Eastern equine encephalitis virus (EEEV), which also acquire opal-to-Cys mutations following passaging in *Dcr2*-deficient C6/36 cells (*9*). Together, our findings demonstrate that *Aedes Dcr2* exerts intense selective pressure to retain the SINV opal codon (Figure 1).

We next tested whether the *in vitro* fitness differences between SINV 550opal and SINV 550C translated into altered infection outcomes in *Aedes* mosquitoes. For this, we used two reagents. The first is a previously published *Aedes aegypti Dcr2* loss-of-function mutant generated by TALEN, in which a constitutively expressed eGFP knock-in cassette is used to disrupt *Dcr2* (*20*). Second, we generated a CRISPR/Cas9-mediated *Dcr2* knockout line with a constitutively expressed *dsRED* inserted into *Dcr2*, thereby disrupting the open reading frame (Figures 2A) (*21*). Trans-heterozygous expression of eGFP and dsRED enables us to visually track the independent insertions in loss-of-function mutants. By crossing the independent heterozygous *A. aegypti* lines, we generated a trans-heterozygous knockout of *Dcr2* (yellow, Figure 2B). We tested *Dcr2* loss-of-function by analyzing survival curves following systemic infection with wild-type SINV (550opal). Consistent with previous data in homozygous *Dcr2*-null eGFP mosquitoes, these trans-heterozygous *Dcr2*-null mosquitoes showed a severe disease phenotype compared to their wild-type siblings (Figure 2C) (*20*, *21*).

We then challenged wild-type or *Dcr2-/-* knockout sibling *A. aegypti* mosquitoes with equivalent doses of wild-type SINV (550opal) or the 550C SINV variant (Figure S3). Consistent with our *in vitro* findings, we found that total viral RNA levels in SINV 550C-infected wild-type mosquitoes were 4-fold lower than those in SINV 550opal-infected wild-type mosquitoes three days post-infection (Figure 2D). This implies that SINV 550C incurs a significant fitness loss in wild-type mosquitoes. As expected, the loss of *Dcr2* significantly improved infection levels for both wild-type SINV (550opal) and SINV 550C. Importantly, SINV RNA levels in 550C-infected *Dcr2-/-* mosquitoes were statistically indistinguishable from viral RNA levels in wild-type SINV (550opal)-infected mosquitoes (Figure 2E).

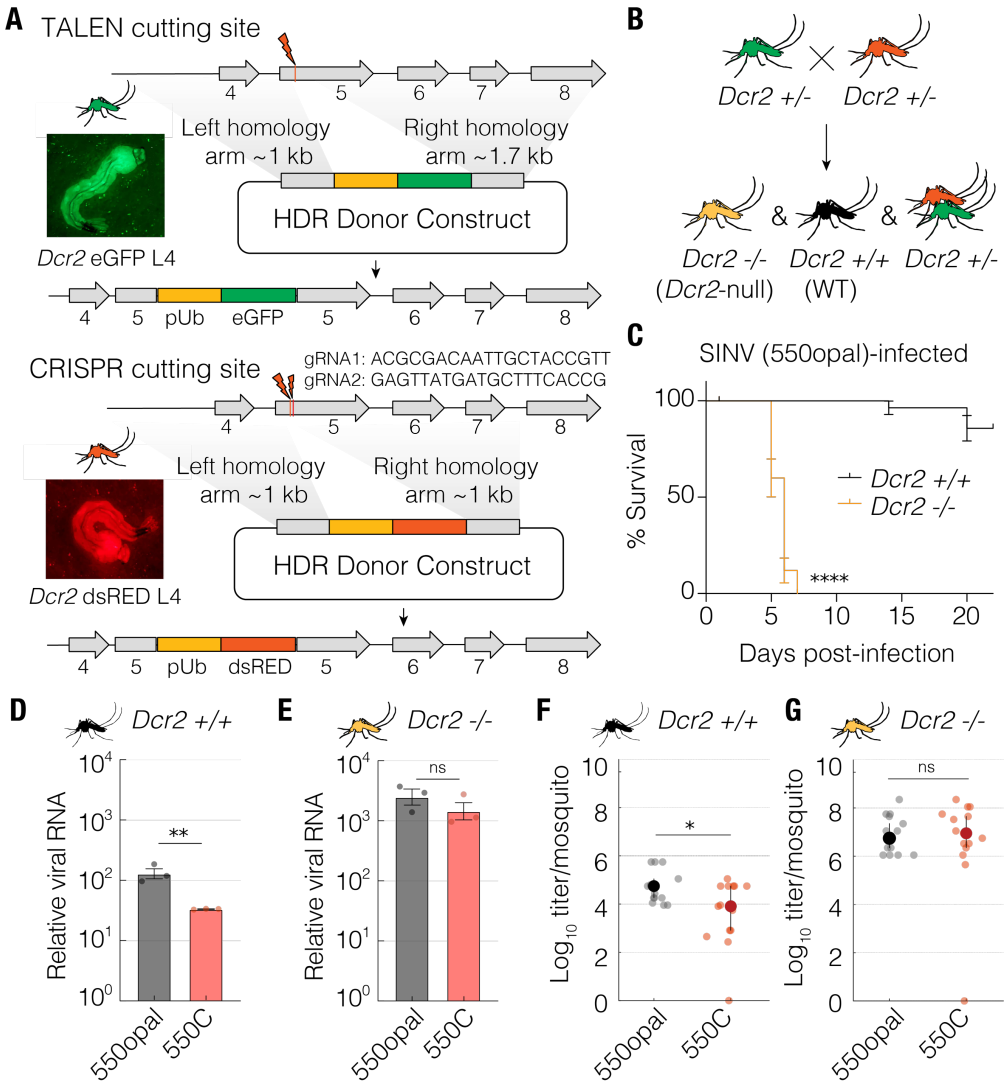

Figure 2. The mosquito RNAi pathway imposes strong selection on SINV nsP3 opal codon *in vivo*. (A-B) (Top) Schematic of TALEN-mediated HDR integration to generate *Dcr2*-null transgenic lines with the knock-in of a frame-disrupting pUb-eGFP marker. (Middle) Schematic of CRISPR-Cas9-mediated *Dcr2*-null transgenic lines with the knock-in of a frame-disrupting pUb-dsRED marker. Photographs are representative of the eGFP or dsRED-expressing mosquitoes selected for crossing experiments **(B)** to generate wild-type (*Dcr2*+/+, black) or trans-heterozygous *Dcr2*-null (*Dcr2*-/-, yellow) mosquitoes (Bottom). **(C)** Survival of sibling wild-type (black line) or trans-heterozygous *Dcr2*-null (yellow line) mosquitoes following systemic SINV infections. Survival curves represent cohorts of ≥28 adult female mosquitoes infected with 10^6 $TCID_{50}$/ml of wild-type SINV (550opal). Significance was determined by log-rank (Mantel-Cox) test, p-value < 0.0001. **(D-E)** Wild-type (*Dcr2*+/+) or *Dcr2*-null (*Dcr2*-/-) *Aedes aegypti* mosquitoes were infected with SINV 550opal or 550C. Three days post-infection, viral RNA was quantified via qRT-PCR. The data represent three independent biological replicates, each consisting of five pooled mosquitoes. Reported values are normalized to 550opal RNA levels in wild-type mosquitoes. **(F-G)** Viral loads were assessed from individual (D) wild-type (*Dcr2*+/+, black) or (E) homozygous *Dcr2*-null (*Dcr2*-/-, yellow) mosquitoes (n=15) collected three days-post infection. Error bars represent the standard error of the mean (SEM). Unpaired t-tests. ** = p < 0.01, * = p < 0.05, ns = not significant.

179 We also assessed *in vivo* viral fitness by quantifying infectious virus titer recovered from infected
180 mosquitoes. In agreement with total viral RNA levels, we recovered five-fold lower amounts of
181 infectious virus from SINV 550C-infected *Dcr2*+/+ mosquitoes compared to those infected with
182 wild-type SINV (550opal) (Figure 2F). As expected, we recovered significantly more infectious
183 virus from *Dcr2*-/- mosquitoes for both viruses (Two-way ANOVA, Tukey's multiple comparison

184 test). In addition, the levels of recovered virus were equivalent between wild-type SINV (550opal)
185 and SINV 550C-infected *Dcr2*-/- mosquitoes (Figure 2G). These findings confirm that the SINV
186 opal codon confers a significant replicative advantage *in vivo,* echoing prior findings from ONNV
187 in *Anopheles gambiae* mosquitoes (*4*). We also show that RNAi loss rescues the *in vivo* fitness
188 defects of the SINV 550C variant (*20*, *21*).

189 **Opal-to-Cys substitution induces higher small RNA response in Dcr2-competent mosquito**
190 **cells**

191 Since SINV 550C exhibits reduced fitness in *Dcr2*+ cells, we hypothesized that this variant might
192 induce a more pronounced siRNA response compared to wild-type SINV (550opal). To test this
193 hypothesis, we performed small RNA sequencing analysis of *Dcr2*+ U4.4 or *Dcr2*– C6/36 cells
194 infected with either 550opal or 550C SINV variants (Figure 3A). *Dcr2 KO* U4.4 cells were not
195 chosen for small RNA sequencing analysis due to the incomplete nature of the knockout.
196 Although SINV 550C infected nearly 10-fold fewer cells compared to wild-type SINV (Figure S4A),
197 virus-derived small RNA levels were significantly elevated in *Dcr2*+ cells infected with SINV 550C
198 relative to those infected with wild-type SINV (550opal) (Figure 3B). Thus, a single nucleotide
199 change (UG<u>A</u> to UG<u>C</u>) in the 11.7 kb SINV genome that leads to the loss of the *nsP3* opal codon
200 is sufficient to trigger a substantially higher small RNA response in mosquito cells.

201 To further dissect the exact nature of the small RNA response, we analyzed small RNAs based
202 on their size distribution and polarity (Figure 3C-F, S4B-E). As expected, the siRNA response
203 against either SINV 550C or SINV 550opal was markedly attenuated in C6/36 cells that lack Dcr2
204 (Figures 3C-D). Moreover, all the small RNAs in C6/36 cells appear to be biased towards the
205 sense strand. However, in Dcr2-competent U4.4 cells, levels of 21-nucleotide vsiRNAs were
206 substantially elevated in SINV 550C-infected cells compared to 550opal-infected cells (Figures
207 3E-F), consistent with SINV 550C's enhanced susceptibility to Dcr2-mediated processing
208 (Figures 3B). We also observed distinct differences in the polarity of siRNAs generated from the
209 two viral variants. The siRNAs derived from 550opal mapped equally to sense and antisense viral
210 RNA, suggesting they originate from double-stranded RNA replication intermediates, in which
211 sense and antisense RNAs are present at equimolar ratios (paired t-test: $p = 0.976$, Figure 3E). In
212 contrast, 550C-derived siRNAs exhibited a strong bias toward the sense strand (paired t-test: p
213 < 0.05, Figure 3F). Our findings indicate that siRNAs generated in SINV 550C-infected cells are
214 more abundant than those generated in wild-type SINV (550opal)-infected cells and originate from
215 single-stranded positive-sense viral RNA instead of double-stranded RNA.

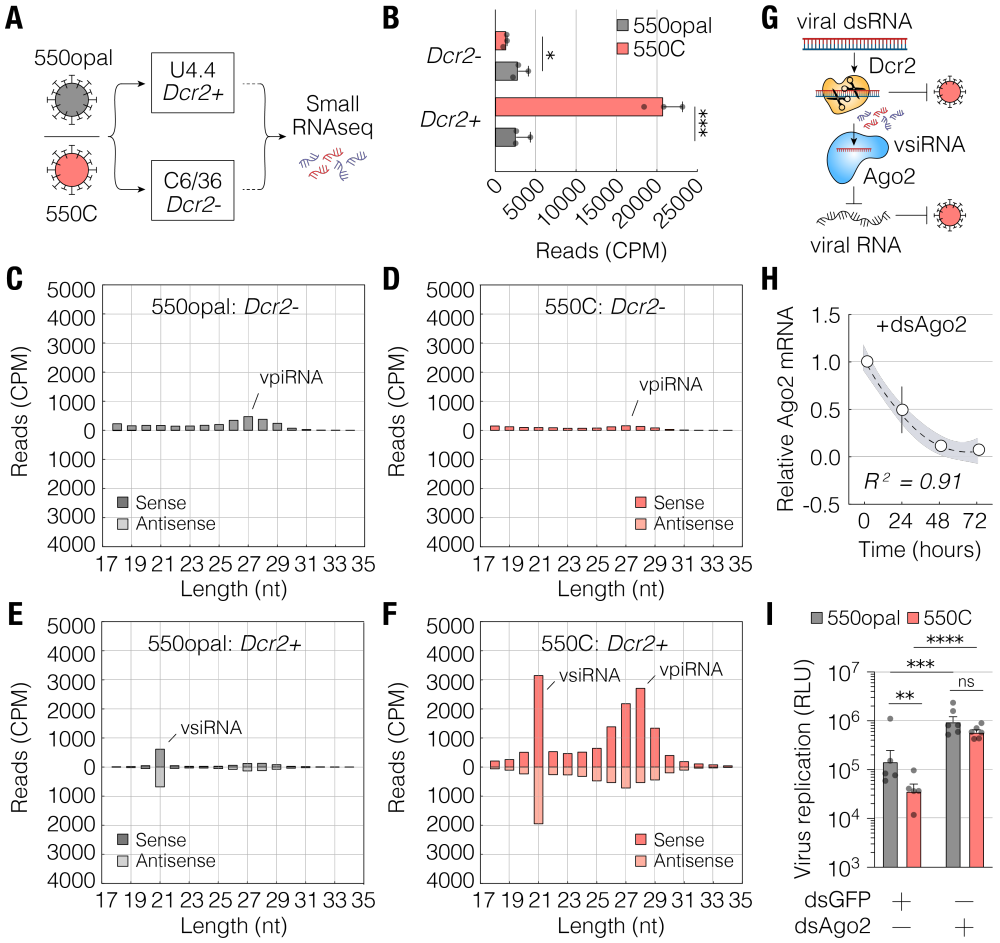

Figure 3. SINV sense-codon variant induces higher small RNA response in mosquito cells. (A) *Dcr2*+ U4.4 or *Dcr2*– C6/36 cells were infected with wild-type SINV 550opal or the SINV 550C variant. Small RNA sequencing was performed on cells collected five days post-infection. **(B)** Normalized small RNA read counts were mapped to SINV genomes in *Dcr2*+ U4.4 or *Dcr2*– C6/36 cells infected with wild-type SINV 550opal and SINV 550C. **(C-D)** Size distribution of small RNAs derived from *Dcr2*- C6/36 cells infected with wild-type SINV 550opal or SINV 550C. **(E-F)** Size distribution of small RNAs derived from *Dcr2*+ U4.4 cells infected with wild-type SINV 550opal or SINV 550C. The data represent three independent biological replicates. **(G)** Schematic of mosquito RNAi pathway and the roles of *Dcr2* and *Ago2* in virus restriction. **(H)** Quantification of relative *Ago2* transcript levels by qRT-PCR in *Dcr2*+ mosquito cells treated with *Ago2* double-stranded RNA (dsAgo2). The dotted line denotes the expected trend from a one-phase exponential decay model. Bands represent the 95% confidence interval. **(I)** Effect of dsAgo2 treatment on the replication of wild-type SINV 550opal and SINV 550C in *Dcr2*+ mosquito cells as quantified by luciferase assay. Error bars represent the standard error of the mean (SEM). Student's t-tests. *** = $p < 0.001$, * = $p < 0.05$, ns = not significant.

We considered two complementary mechanisms by which higher siRNA production during SINV 550C infection in Dcr2-competent U4.4 cells could directly reduce fitness (Figure 3G, top). First, Dcr2-mediated cleavage of viral dsRNA could be inherently damaging to the virus due to the loss of minus-strand replication template. This would result in a stoichiometric reduction of intact viral dsRNA, which by itself might be sufficient to lower viral fitness. Alternatively, viral siRNAs generated by Dcr2 can be targeted to degrade nascent viral RNA via Argonaute 2 (Ago2), thereby restricting viral replication (Figure 3G, bottom). To distinguish between these two mechanisms, we tested whether Ago2-mediated targeting of vsiRNAs to viral RNAs is necessary for SINV 550C inhibition. To achieve this, we performed *Ago2* knockdown using double-stranded RNA (dsRNA) against *Ago2* in U4.4 cells, resulting in >90% knockdown within 48 hours (Figure 3G-H, Figure S5A). If both cleavage and Ago2 targeting played substantial antiviral roles, then we would expect that an *Ago2* knockdown would have had only a modest impact on viral fitness (Figure 3G). In

contrast to this expectation, we found that *Ago2* knockdown substantially increased SINV 550C replication to levels indistinguishable from those of wild-type SINV (550opal) (Figure 3I). This result demonstrates that the subsequent Ago2-mediated vsiRNA targeting of viral RNA substantially contributes to the loss of SINV 550C fitness in *Dcr2*+ cells.

In addition to vsiRNAs, we also found viral-derived 24-31nt piwi-interacting RNAs (piRNAs) in both C6/36 and U4.4 cells, similar to previous studies (Figures 3C-F, S6, S7, S8A) (*14*, *15*, *22*, *23*). In mosquito cells, viral piRNAs (vpiRNAs) are predominantly generated via a ping-pong-like mechanism that utilizes specific PIWI proteins, such as Ago3 and Piwi5 (*24*). Consistent with previous studies, we found that SINV-derived piRNA reads originated primarily from the subgenomic RNA, particularly from a hotspot at the 5' end of the capsid gene (Figure S6B) via a canonical ping-pong amplification pathway (Figure S8C) (*23*). Just like siRNAs, we found that C6/36 cells accumulate significantly fewer viral-derived piRNAs than U4.4 cells (Figures 3C-F, S8A-B). *Dcr2*+ U4.4 cells infected with the SINV 550C variant also accumulate 24-31nt long viral-derived piRNAs at 12-fold higher levels than the wild-type SINV variant (Figures 3B-C and S8A). In contrast, SINV 550C infection is associated with a 2-fold reduction in small RNAs in mosquito cells lacking *Dcr2*, which exhibit a near-complete lack of vsiRNA and vpiRNA production (Figure 3E-F). Thus, even though vpiRNA production is canonically thought to be independent of mosquito *Dcr2* activity, our results add to a growing body of evidence that suggests a functional crosstalk between the siRNA pathway and the production of ping-pong generated piRNAs in mosquitoes (*22*, *25–27*). Unlike viral-derived siRNAs, which have been previously shown to restrict alphavirus replication in insect cells, the antiviral role of viral-derived piRNAs is more ambiguous (*25*, *28*). In our study, we did not observe any significant changes in levels of the subgenomic RNA template or structural protein expression between wild-type SINV (550opal) and SINV 550C-infected *Dcr2*+ cells (Figure S8D). Moreover, since knockdown of *Ago2*, which is involved in siRNA but not piRNA targeting, was sufficient to restore the fitness of the SINV 550C variant to wild-type levels in U4.4 cells (Figure 3I), we conclude that viral-derived piRNAs do not play a substantial antiviral role and do not discuss them further in this study.

SINV Structured RNA element protects against RNAi in mosquito cells

To determine whether specific SINV genomic regions act as Dicer 2 substrates in wild-type SINV and particularly SINV 550C-infected cells, we mapped all 21-nt vsiRNA reads to the SINV reference genome. Using a 40-nucleotide sliding window in the SINV genome, we identified regions with higher-than-average vsiRNA coverage (Figure 4A). Since infection by the SINV 550C variant elicited a more robust siRNA response than wild-type SINV (550opal), we primarily focused on identifying SINV genomic regions that showed disproportionately higher vsiRNA coverage in SINV 550C compared to wild-type SINV (550opal) (Figure 4B). This differential analysis revealed several windows in the SINV genome that produced disproportionately more vsiRNAs during infection with the SINV 550C variant. The most striking of these was a 23-nt stretch within the E1 structural gene coding region. This 'hotspot', which we designated E1-hs, represented more than 4% of total siRNA reads in SINV 550C (99.85th percentile). E1-hs is also a hotspot in SINV 550opal, producing 1% of total siRNA reads (96th percentile) (Figures 4A-B).

The SINV RNA genome comprises several structural RNA elements essential for its replication, expression, and packaging (*29*). Due to the biased polarity of vsiRNAs derived from SINV 550C, such structural RNA elements could be hotspots for producing disproportionately large amounts of viral-derived siRNAs. Indeed, the vsiRNA reads mapping to the E1-hs region exhibited a severe bias toward the sense strand (Figure 4A inset). This suggested that these E1-hs siRNAs may have been derived from some structured RNA element in the SINV genome. To investigate the possibility that E1-hs corresponds to structured RNA, we analyzed previously generated SINV RNA SHAPE-MaP data to calculate and plot the density distribution of median SHAPE reactivity values using the same 40-nucleotide sliding window across the SINV genome (*30*). Residues within the E1-hs region exhibited distinctly negative SHAPE reactivity values, indicating they are a part of highly structured RNA in SINV (Figure 4C). We assessed the evolutionary conservation

of this RNA secondary structure by performing secondary structure prediction using aligned sequences of the E1-hs region from different mosquito-isolated alphaviruses and by referencing prior SHAPE-MaP data collected from Chikungunya virus (CHIKV), which is distantly related to SINV (*31*). Our analyses revealed a high degree of primary sequence conservation in the E1-hs element (Figure S9). Although some of this conservation may result from constraints on the E1 coding region, we also observed a high degree of covariance between paired residues that form a stem-loop structure, which is more consistent with evolutionary constraints to maintain a structural RNA element. We also compared the genome-wide vsiRNA profiles between SINV 550C and SFV, using data previously collected from SFV4-infected *Dcr2*+ U4.4 *(Aedes albopictus)* and Aag2 *(Aedes aegypti)* cells (*15*). Our comparison revealed several hotspots of vsiRNA production, including the SINV E1-hs region, that were shared between the two viruses despite their high overall sequence divergence (Figure S10A-B) (*15*).

To test the functional significance of the E1-hs hotspot, we introduced synonymous mutations that disrupt the E1-hs secondary structure without altering the E1 protein-coding sequence (Figure 4D). We then compared the replication efficiency of these E1-hs$_{mut}$ variants with that of their wild-type counterparts in both SINV 550C and SINV 550opal viruses in *Dcr2*– (C6/36) cells (Figure 4E). In *Dcr2*– cells, we found that SINV E1-hs$_{mut}$ replication was indistinguishable from that of wild-type SINV. Similarly, the replication of SINV 550C E1-hs$_{mut}$ was indistinguishable from SINV 550C in *Dcr2*– cells. Thus, E1-hs$_{mut}$ variants do not intrinsically impair viral replication. We then investigated the effect of the E1-hs mutation in *Dcr2*+ cells (Figure 4F). We found that the

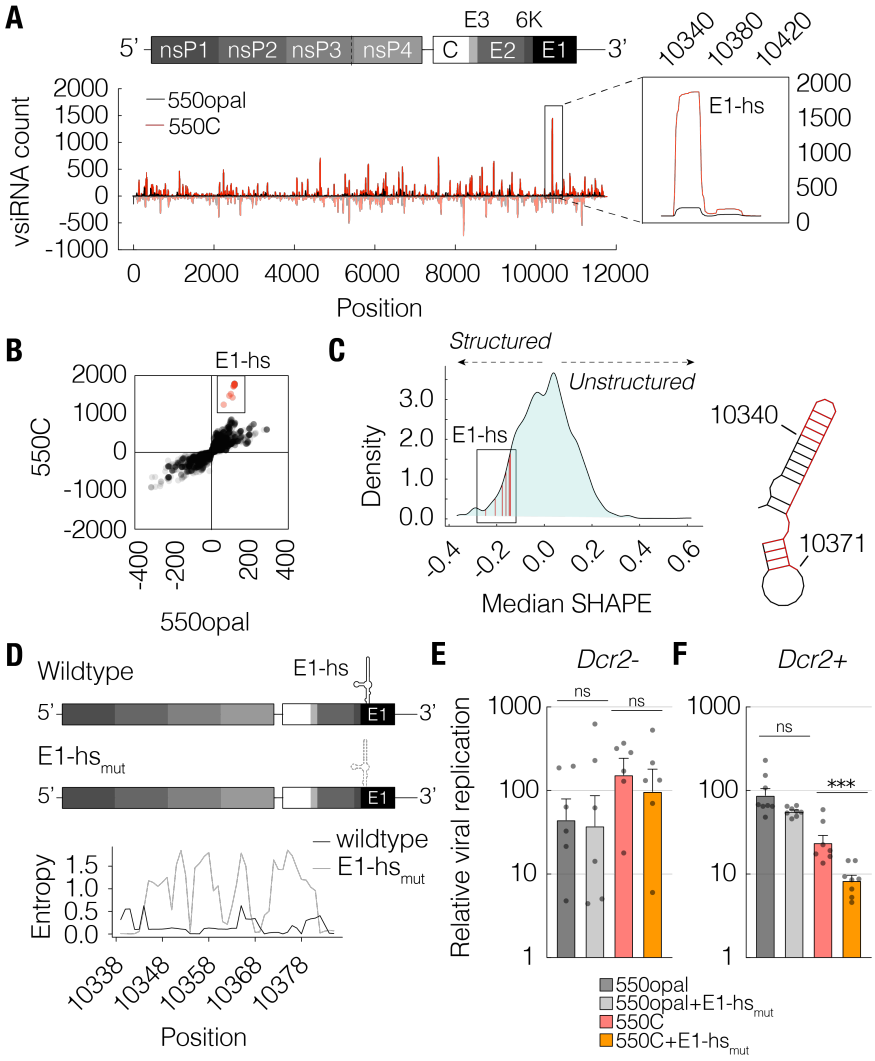

Figure 4. A structured RNA element enables SINV to blunt the siRNA response. (A) Distribution of vsiRNA reads from wildtype SINV 550opal (in black) or SINV 550C (in red) viruses in *Dcr2*+ U4.4 cells. Positive and negative Y-axis values represent read counts mapped to the sense and antisense strands, respectively, at every position along the SINV genome (X-axis). The inset shows a zoomed-in view of the E1-hs region. **(B)** Correlation of per-site vsiRNA reads mapped to wildtype SINV 550opal or SINV 550C viruses. Residues within the E1-hs region are boxed and colored in red. **(C)** Density distribution profile of median SHAPE values of SINV RNA. Median SHAPE values of residues within the E1-hs region are boxed and highlighted in red. Location of the E1-hs region in SHAPE-constrained RNA secondary structure. **(D)** Schematic of viral genomes with intact (wildtype) and mutated E1-hs (E1-hs$_{mut}$). Positional entropy profile of E1-hs RNA structural element in wild-type SINV and the E1-hs$_{mut}$ strain. High and low entropy values indicate conformationally flexible and rigid structure, respectively. **(E)** Replication of wildtype SINV 550opal or SINV 550C viruses with intact or destabilized E1-hs structure in *Dcr2*– C6/36 cells as quantified via luciferase reporter assays. The data represent six independent biological replicates. **(F)** Replication of wildtype SINV 550opal or SINV 550C viruses with intact or destabilized E1-hs structure in *Dcr2*+ U4.4 cells. The data represent six independent biological replicates. Two-way ANOVA with Tukey's multiple comparisons test. **** = $p < 0.0001$, *** = $p < 0.001$, * = $p < 0.05$, ns = not significant.

replication of the SINV E1-hs$_{mut}$ variant was comparable to that of wild-type SINV in *Dcr2*+ cells. In contrast, we found that SINV 550C E1-hs$_{mut}$ replicated to significantly lower levels than SINV 550C in *Dcr2*+ cells (Figure 4F). Thus, the ability of E1-hs to overproduce siRNAs is crucial for maintaining the fitness of the 550C variant in *Dcr2*+ cells since the SINV 550C genome is more susceptible to Dcr2 targeting. Our findings indicate that the SINV opal codon and the E1-hs structure function synergistically as a multipotent RNAi evasion strategy.

Disrupted nsP processing compromises the integrity of viral replication spherules and leads to higher RNAi susceptibility

We next asked why the SINV 550C variant is so much more susceptible to RNAi than wild-type SINV (550opal). We previously found that opal-to-sense substitutions lead to overproduction of the full-length nsP (P1234), which disrupts polyprotein processing kinetics. These disparities in polyprotein processing between wild-type SINV and sense-codon variants are most pronounced in vertebrate cells cultured at 37°C, but also manifest (albeit to a lesser extent) in both vertebrate and mosquito cells maintained at 28°C (*1*). In particular, less P123 is produced early during infection in SINV 550C-infected *Dcr2*+ cells, presumably due to delayed P3/4 processing caused by excess P1234 (Figure S11A-B). We therefore considered the possibility that functional RNAi might exacerbate delays in polyprotein processing. However, we observed similar polyprotein processing trends in *Dcr2*+ (U4.4) and *Dcr2*– (C6/36) mosquito cells at 28°C (Figure S11A and C, S11B and D), ruling out the possibility that RNAi status affected SINV nsP polyprotein processing.

Next, we considered whether the increased RNAi susceptibility of the SINV 550C variant was due to increased viral dsRNA production, which could lead to higher antiviral vsiRNA output in *Dcr2*+ cells. This increase in dsRNA could result directly from the nsP processing defect, which delays transitions from minus-strand to plus-strand replication. We have previously employed a quantitative RT-PCR (qRT-PCR) assay to quantify intracellular levels of SINV genomic RNA, including both the plus and minus strands (*1*). However, we were concerned that Dcr2 cleavage of viral dsRNA might preclude accurate estimation of viral dsRNA levels within cells. Therefore, to detect both intact and potentially processed dsRNA, we employed the J2 monoclonal antibody, which has been well-characterized for detecting both longer and shorter dsRNAs, ranging in length from 14 to 40 bp (*32*, *33*). We performed immunofluorescence microscopy on *Dcr2*+ (U4.4) cells, which revealed distinct J2 foci in the cytoplasm of SINV-infected cells, but not in uninfected cells. These J2 foci indicate SINV replication compartments (RCs) or spherules (Figure 5A). We quantified J2/dsRNA intensity within these spherules. While there were no changes in total spherule counts per cell, we found that *Dcr2*+ (U4.4) cells infected with SINV 550C have a 29% increase in spherule J2 intensity compared to those infected with wild-type SINV (550opal), suggesting that SINV 550C replication spherules contain more J2-binding dsRNA substrate (Figure 5B-C).

Recent cryo-EM reconstruction of wild-type alphavirus replication organelles showed that each spherule contains only a single copy of full-length viral dsRNA (*34*). We therefore wondered whether the accumulation of Dcr2-processed dsRNA fragments could lead to an increase in spherule J2 intensity in SINV 550C-infected *Dcr2*+ cells. To test this possibility, we performed a similar analysis in *Dcr2*- C6/36 cells (Figure S12A). We reasoned that if SINV 550C inherently synthesizes excess full-length dsRNA, then we would also expect to see a similar increase in spherule J2 signal in cells lacking Dcr2. However, we found no significant differences in spherule J2 intensities between wild-type and SINV 550C-infected C6/36 cells (Figure S12B-C). These findings confirm both our previous small RNAseq analyses of greater siRNA production in SINV 550C-infected U4.4 cells and our hypothesis that the increased spherule J2 signal in SINV 550C-infected U4.4 cells (Figure 5B-C) represents an excess of processed dsRNA fragments.

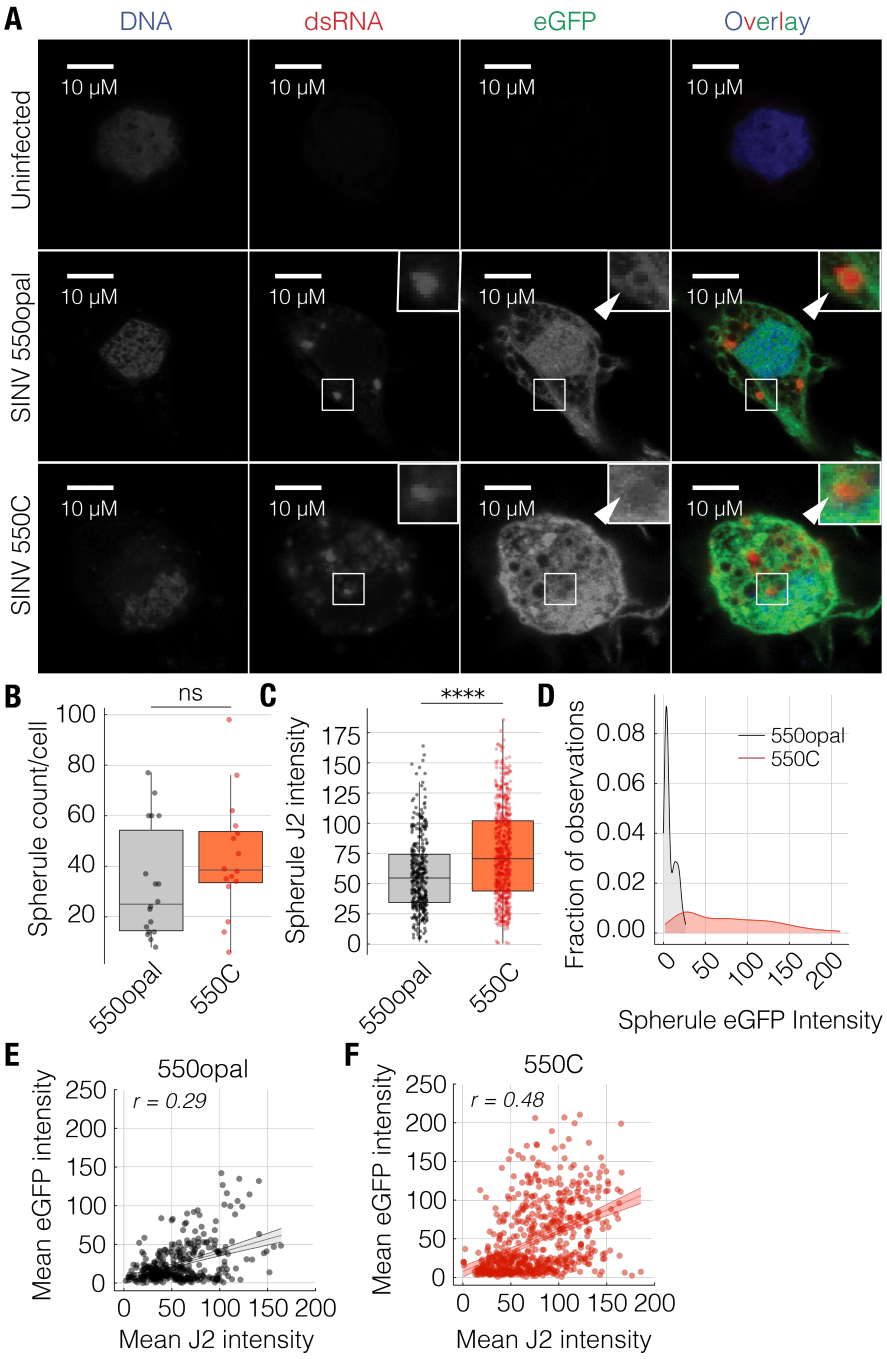

Figure 5. Delayed non-structural polyprotein processing in SINV 550C compromises the integrity of viral replication spherules. (A) Confocal microscopy-based localization of viral dsRNA (J2) and virally encoded eGFP in *Dcr2*+ U4.4 cells that were either uninfected (top row), infected with wild-type SINV 550opal (middle row), or infected with SINV 550C (bottom row). The inset shows the localization of eGFP and dsRNA around (middle row) or within (bottom row) viral replication spherules. White arrows indicate spherule outer boundaries. **(B)** Spherule count per cell is reported as the mean number of spherules per cell in each z-stack. **(C)** Quantification of J2 intensities within viral replication spherules (n=629) in *Dcr2*+ U4.4 cells infected with either wild-type SINV 550opal or SINV 550C. Mann-Whitney U test. **** = $p < 0.0001$, ns = not significant. Error bars represent the standard error of the mean (SEM). **(D)** Density distributions of observed values of spherule eGFP intensity in wild-type SINV 550opal or SINV 550C-infected *Dcr2*+ cells. Kolmogorov-Smirnov (KS) test = 0.862, $p < 0.0001$. **(E-F)** Correlation between mean dsRNA and eGFP intensities per spherule across *Dcr2*+ cells infected with either wild-type SINV 550opal or SINV 550C. Spearman's correlation tests (E-F: $p < 0.0001$).

Another consequence of the nsP processing defects in cells infected by the SINV 550C variant could be the compromised integrity of mature viral replication spherules, which are comprised of processed non-structural proteins. Initial alphavirus replication spherule formation requires the intact P123 polyprotein, while spherule maturation requires further processing into nsPs 1-4 (*35–37*). Replication spherule formation is a passive but highly effective viral evasion strategy by occluding viral dsRNA replication intermediates from cellular RNA sensors and effectors, including Dcr2 (*38*, *39*). Presence of processed dsRNA within or proximal to replication spherules in SINV 550C-infected *Dcr2*+ cells suggested a scenario in which mature spherule formation is delayed in SINV 550C due to aberrant processing of P123 polyprotein, which reduces the structural integrity of replication complexes and allows cytoplasmic Dcr2 to access and cleave viral dsRNA. To test this hypothesis, we quantified spherule integrity by measuring their ability to occlude virally encoded cytoplasmic eGFP. If viral spherule integrity were maintained, we would expect to see occlusion of the otherwise freely diffusing cytoplasmic eGFP. Indeed, 2D plot profile analysis of dsRNA-containing intact spherules (identified using the J2 antibody) in *Dcr2*+ cells infected with wild-type SINV (550opal) revealed a noticeable decline in eGFP intensity within spherules relative to regions outside the spherule boundary, consistent with the selective exclusion of cytoplasmic eGFP from the viral spherule compartment (Figure S12D). In contrast, within-spherule GFP intensity was noticeably higher in SINV 550C-infected cells. Upon assaying a larger number of J2-marked viral replication spherules in *Dcr2*+ cells infected with wild-type SINV (550opal), we found a bimodal distribution of spherule eGFP intensity values: most spherules exclude eGFP entirely, whereas only a very small subpopulation of spherules cannot exclude eGFP (Figure 5D). In contrast, in SINV 550C-infected cells, spherule eGFP intensity values showed a wider unimodal distribution, indicating significantly greater eGFP-leakage into spherules (Figure 5D). Thus, in SINV 550C-infected cells, few viral replication spherules can exclude eGFP, whereas most spherules cannot. We also observed a positive correlation between J2 intensity and eGFP intensity within individual spherules in wild-type SINV-infected *Dcr2*+ cells (Figure 5E). This correlation was stronger in SINV 550C-infected cells, indicating that compromised spherule integrity is associated with higher levels of processed dsRNA within a subset of spherules (Figure 5F).

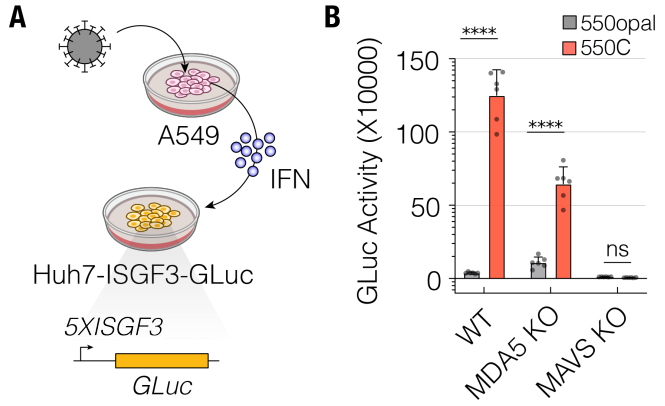

Figure 6. SINV sense-codon variant induces higher IFN response in human cells. (A) A549 cells were infected with either wild-type SINV 550opal or SINV 550C at an MOI of 5. Huh7 cells with a 5XISGF3-GLuc reporter were treated for 18h with A549 cell supernatants before the quantification of secreted GLuc. **(B)** Reporter activity in 5XISGF3-GLuc Huh7 cells treated with supernatants collected from wild-type, *MDA5* KO, or *MAVS* KO A549 cells infected with either wild-type SINV 550opal or SINV 550C at 16 hours post-infection. The data represent the mean of six independent biological replicates. Two-way ANOVA with Sidak's multiple comparisons test. **** = $p < 0.0001$, ns = not significant.

SINV Opal-to-Cys variant induces higher interferon response in vertebrate cells

Our previous study demonstrated that the nsP processing defects of the SINV 550C variant also occur in vertebrate cells (*1*). Unlike insects, RNAi is not the predominant immune defense pathway in vertebrate cells. Instead, viral RNA is detected by host-encoded pattern recognition receptors (PRRs) RIG-I and MDA5, which recognize viral dsRNA to trigger downstream interferon (IFN) responses (*40*). Based on our findings that nsP processing delays result in spherule integrity defects in mosquito cells, we hypothesized that similar spherule defects occur during SINV 550C infection in vertebrate cells. Thus, although the vertebrate cells used in our prior study lacked innate immunity, we reasoned that nsP processing defects in immune-competent cells might activate

vertebrate dsRNA sensors, leading to differential induction of innate immune responses. If this were the case, we would expect that SINV 550C-infected cells would trigger a stronger interferon response than wild-type SINV (550opal)- infected cells. We tested this hypothesis by infecting human A549 cells with either SINV 550C or SINV 550opal for 16 hours and measuring IFN production in Huh7 cells expressing a 5XISGF3-GLuc reporter (Figure 6A) (*41*). Consistent with our expectation, we observed significantly higher GLuc activity from cells treated with supernatants collected from SINV 550C-infected A549 cells compared to those treated with wild-type SINV (550opal)-infected A549 cell supernatants (Figure 6B).

A549 cells respond to dsRNA by upregulating the expression of RIG-I and MDA5 (*42*). Both of these PRRs are crucial for IFN induction in response to alphavirus infection, and signal through the Mitochondrial Antiviral Signaling protein (MAVS) (*43*). We therefore tested whether sensing via MDA5, the cytoplasmic RNA sensor implicated in sensing long double-stranded RNA (dsRNA), is responsible for the elevated interferon induction observed in response to SINV 550C infection in human cells. We infected *MDA5* KO A549 cells with either SINV 550C or wild-type SINV (550opal) and measured the resulting interferon response at 16 hours post-infection (hpi). We found that MDA5 loss significantly reduced IFN production from SINV 550C-infected A549 cells (Figure 6B). However, the loss of MAVS (*MAVS* KO) further reduced IFN production from SINV 550C and wild-type SINV (550opal)-infected A549 cells (Figure 6B). Together, these results suggest that MDA5 cooperates with other RLRs to sense SINV 550C RNA when spherule integrity is compromised and signals through MAVS to trigger interferon production.

Collectively, our data support a model in which delayed nsP processing, caused by Opal-to-Cys substitutions at the stop codon between nsP3 and nsP4, leads to the formation of defective or incompletely formed spherules in alphavirus-infected cells (Figure 7). These structurally compromised spherules enable cytoplasmic proteins, including cytoplasmic RNA sensors such as Dcr2 in insect cells and MDA5 in vertebrate cells, to access viral dsRNA, thereby enhancing immune activation and ultimately lowering viral fitness in immune-competent insect and vertebrate cells (Figure 7B). Thus, the nearly universally conserved nsP3 opal codon in alphaviruses is critical to cloak viral RNA replication so it does not trigger host immunity in both insect and vertebrate hosts.

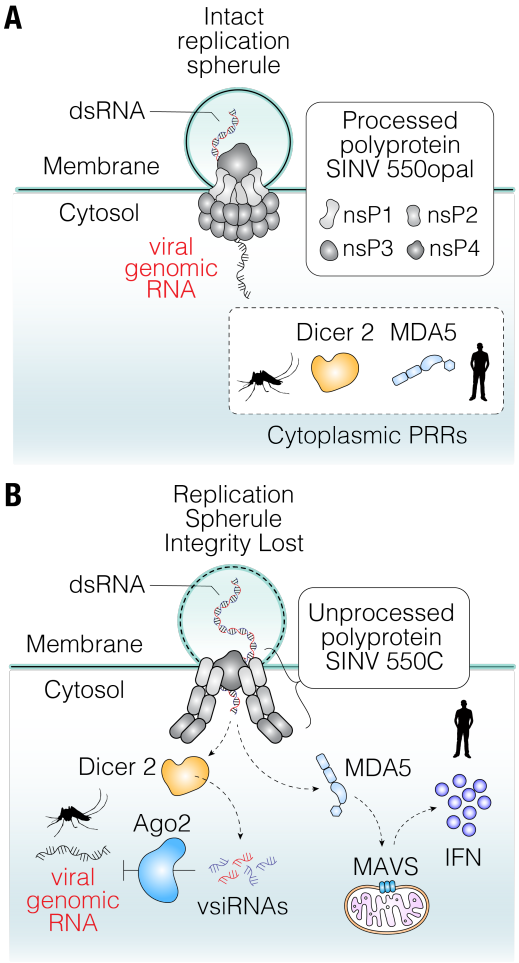

Figure 7. Proposed model by which opal-to-sense codon substitutions lower viral fitness. (A) SINV nsP3 opal codon helps maintain replication spherule integrity to avoid detection of viral RNA by cytoplasmic RNA nucleases (Dcr2) or sensors (MDA5) in mosquito or vertebrate cells, respectively. **(B)** Improper processing of the nsP polyprotein in SINV 550C variant-infected cells leads to the loss of spherule integrity, resulting in excessive Dcr2 and Ago2-mediated antiviral RNAi induction in mosquito cells and MDA5-mediated, MAVS-dependent IFN induction in vertebrate cells.

Discussion

Our study demonstrates that the retention of the highly conserved nsP3 opal stop codon is a multipotent defensive strategy employed by alphaviruses (Figure 7A). By systematically dissecting its function in both insect and vertebrate cells, our

findings reveal that the opal codon is essential not only for a temperature-dependent trade-off between nsP production and processing, as we previously showed (*1*), but also for maintaining the physical integrity of replication spherules to safeguard viral dsRNA from host immune sensors. We find that opal-to-sense substitutions (e.g., SINV 550C) disrupt the cadence of alphavirus non-structural polyprotein processing, leading to the formation of spherules with potentially compromised integrity and consequently increased exposure of viral dsRNA (Figure 7B). This defect enables cytoplasmic Dcr2 in mosquitoes to access and process viral dsRNA, triggering a much more robust antiviral siRNA response that sharply reduces viral fitness in RNAi-competent *Aedes albopictus* cell lines and *in vivo* in *Aedes aegypti* mosquitoes (Figures 1B, 2C-F, 7B). Using small RNA sequencing, we show that SINV 550C, which differs from wild-type SINV by a single nucleotide at the opal codon, induces significantly higher small RNA response in *Aedes albopictus* cells (Figure 3B). This direct measurement of RNAi activity in response to wild-type and variant SINV infections provides conclusive evidence for the role of RNAi in the fitness advantage conferred by the opal codon. These findings expand on earlier work in *Anopheles gambiae*, where an Opal-to-Arginine mutation reduced ONNV infectivity, underscoring the evolutionary importance of preserving the opal codon for efficient vector transmission (*4*). We also show that alphaviral structural RNA elements, such as E1-hs, protect viral fitness against host RNAi by acting as 'decoy' hotspots of vsiRNA production, likely blunting the antiviral RNAi response (Figure 4). Thus, alphaviruses use a two-pronged defense strategy against mosquito RNAi: first, by physically sequestering dsRNA within replication spherules, and second, by producing 'decoy' vsiRNAs from structured genomic RNA elements. Beyond insects, compromised spherule integrity in vertebrate cells may also permit RNA sensors, such as MDA5, to detect viral dsRNA, thereby enhancing interferon signaling (Figure 6B, 7B).

Recent *in situ* structural and functional characterization has provided insights into the architecture of mature alphavirus replication spherules – membrane-associated structures that shield the viral dsRNA from cytoplasmic RNA-sensors in vertebrate and mosquito cells (*34*, *44–47*). While the process of mature spherule biogenesis remains poorly understood, it is thought to require proteolytic processing of P1234 into nsP1-4 proteins that comprise the 'neck' of the replication spherule (*2*, *35*, *36*, *44*, *48*). Using quantitative western blotting and confocal microscopy, we show that incomplete polyprotein processing in SINV 550C disrupts the structural integrity of replication spherules, potentially allowing cytoplasmic Dcr2 access to viral dsRNA in infected mosquito cells (Figures 5, S11). Additionally, the J2 signal intensity in SINV 550C-infected cells is higher than that in cells infected with wild-type SINV (550opal), but only in the presence of Dcr2, suggesting that the excess J2 signal may represent Dcr2-processed viral dsRNA, contributing to the overall increase in the siRNA response (Figures 5C, S12B-C). Therefore, increased vsiRNA induction by SINV 550C is correlated with slower processing of viral nsP (Figure S11). However, we could not determine whether the higher RNAi induction in SINV 550C-infected mosquito cells is due to Dcr2 gaining access to the viral replication compartment or to viral dsRNA leaking from spherules into the host cytoplasm.

Together, these findings suggest that while some opal-to-sense substitutions may promote viral replication in Dcr2-deficient mosquito cells, the resulting delay in polyprotein processing may compromise the integrity of replication spherules. This structural vulnerability increases viral susceptibility when Dcr2 is present, ultimately limiting the replication efficiency of sense-codon variants in Dcr2-competent cells. Our results mirror previous findings of a Dcr2-dependent change in the relative replication of CHIKV replicons carrying mutations that delay nsP processing, potentially suggesting a generalizable trade-off between replication efficiency and RNAi susceptibility (*49*).

Given that RNAi is the primary antiviral defense mechanism in mosquitoes, mosquito-transmitted viruses have evolved several mechanisms to circumvent or suppress the RNAi response while maintaining persistent, non-pathogenic infections in their vectors. For example, non-coding subgenomic flaviviral RNAs (sfRNAs) present at the 3' end of flavivirus genomes outcompete native Dcr2 and Ago2 substrates for binding, leading to decreased RNAi activity (*50*). Other

502 viruses, such as Flock House virus (FHV B2, *Nodaviridae)* and Culex Y virus (CYV VP3,
503 *Birnaviridae),* encode *bona fide* viral suppressors of RNAi (VSRs) (*51–53*). Alphaviruses are not
504 known to encode sfRNAs or proteins with strong VSR activity, with the possible exception of
505 CHIKV nsP2/3 and SFV capsid, which weakly suppresses RNAi in mammalian cells by potentially
506 sequestering viral dsRNA (*54*, *55*). SINV expressing heterologous FHV B2 exhibits high vector
507 mortality and reduced virus transmission (*56*). Thus, it is likely that, unlike other arboviruses,
508 alphaviruses avoid strong, direct RNAi suppression. Instead, they may dampen or evade the
509 mosquito RNAi response rather than completely block it, thereby maintaining persistent, nonlethal
510 infection in insect hosts.

511 Our current understanding of how alphaviruses suppress mosquito RNAi is based on a study
512 using Semliki Forest Virus (SFV), which is unusual among alphaviruses because it predominantly
513 lacks the nsP3/4 opal stop codon (*15*). SFV genomes produce 'decoy' vsiRNAs during infection
514 in mosquito cells that overwhelm the RISC machinery, protecting RNAi-susceptible viral targets.
515 These vsiRNAs are derived from genomic hotspots that correspond to structured RNA regions,
516 but they are not antiviral themselves. Consistent with this 'decoy' vsiRNA model, we identified a
517 vsiRNA hotspot in SINV, which maps to a structured RNA element within the E1 coding region
518 (Figures 4A-C). Increased RNA exposure in SINV 550C-infected cells disproportionately affects
519 vsiRNA production from this hotspot element (Figure 4A-inset). Disrupting this RNA secondary
520 structure (E1-hs) significantly reduced SINV 550C replication in RNAi-competent cells,
521 underscoring its role in RNAi evasion (Figures 4D and F). Structural conservation of this RNA
522 element also suggests that it may perform a similar function in other alphaviruses (Figure S9).
523 Although such decoy strategies can be generally beneficial, our findings that mutations in E1-hs
524 specifically lower the fitness of the SINV 550C variant demonstrate that they are especially critical
525 when viruses are more susceptible to Dcr2 inhibition due to defects in spherule integrity, which
526 might be caused by genetic mutations (as we show in this study) or by other biophysical changes
527 within host cells.

528 Our current results also expand our previous model, in which the nsP3 opal codon helps balance
529 alphavirus polymerase (RdRp) production and nsP processing efficiency in vertebrate cells (*1*).
530 We now demonstrate that the opal codon also serves a mosquito-specific function by enabling
531 alphaviruses to avoid triggering an antiviral siRNA response (Figure 7). It may also explain why
532 the opal codon is strictly retained across insect-restricted alphaviruses that do not face any
533 vertebrate- or temperature-specific constraints described in our previous study (*1*). Furthermore,
534 compromised replication spherule integrity in SINV 550C also leads to increased recognition by
535 the cytoplasmic RNA sensor MDA5 in mammalian cells, resulting in increased IFN induction
536 (Figure 6B) (*43*).

537 Opal-to-sense mutations are extremely rare in SINV strains. To date, only the AR86 strain of SINV-
538 like virus has been shown to carry an Opal-to-Cys mutation, which co-occurs with a non-
539 synonymous mutation (nsP1 I538T) near the P1/2 cleavage site (*19*). Previous studies have
540 demonstrated that this co-occurring nsP1 I538T mutation helps suppress the vertebrate Type I
541 IFN response by inactivating STAT1/2, which contributes to its neurovirulence (*57*, *58*). We
542 recently demonstrated that the SINV I538T mutation helps restore the disruption in nsP
543 processing cadence caused by the Opal-to-Cys mutation by a 'double delay' (*1*). However, such
544 a 'double delay' may not ameliorate but instead exacerbate spherule integrity defects. Our
545 observation that SINV 550C also induces a higher IFN response suggests the intriguing possibility
546 that the nsP1 I538T mutation in SINV AR86 may have been selected to help counteract the
547 elevated IFN response induced via the Opal-to-Cys mutation.

548 One of the central conflicts faced by viruses infecting evolutionarily divergent host species is that
549 adaptations that provide fitness benefits in one host, such as vertebrates, may prove deleterious
550 in another host, such as mosquitoes (*59–65*). Other viral adaptations might confer benefits in both
551 hosts. Our study highlights one adaptation – the nsP3 opal codon – that provides a benefit in both
552 hosts by maintaining replication spherule integrity, thereby protecting viral RNA from cytoplasmic

553 nucleases and sensors in both insect and vertebrate hosts (Figure 7). In so doing, this single
554 codon confers a fitness advantage in RNAi-competent mosquito cells while also limiting interferon
555 responses in mammalian cells. Thus, the retention of the opal codon by alphaviruses reflects
556 evolutionary pressure from immunity in both hosts. By demonstrating that the alphavirus opal
557 codon is a multipurpose defensive adaptation, our work reframes a classical paradigm of
558 alphavirus biology and opens new avenues for research into vector-borne disease control.

559 **Materials and Methods**

560 *Insect and Mammalian Cell Culture*

561 C6/36 *Aedes albopictus* cells were grown at 28ºC under 5% CO_2 in humidified incubators and
562 were cultured in high-glucose, L-glutamine Minimal Essential Medium (Gibco) supplemented with
563 10% fetal bovine serum (Cytiva) and 1% penicillin-streptomycin (Gibco). U4.4 *Aedes albopictus*
564 cells were grown at 28ºC under 5% CO_2 in humidified incubators. They were cultured in high-
565 glucose, L-glutamine Mitsuhashi and Maramorosch Insect Medium w/o Sodium bicarbonate
566 (VWR) supplemented with 0.12gm/L Sodium bicarbonate, 10% fetal bovine serum (Cytiva), and
567 1% penicillin-streptomycin (Gibco). The *Aedes albopictus* U4.4 cells were a gift from Dr. Douglas
568 (Doug) Brackney (University of Connecticut).

569 *CRISPR editing of Dicer 2 in U4.4 cells*

570 $5X10^5$ U4.4 cells seeded into 6-well plates were co-transfected with 6.25 µg purified SpyCas9-
571 NLS (PNA Bio #CP01-50) and synthesized single guide RNA (sgRNA)
572 (AUAUUCGACGAAUGUCACCA) targeting the 5' end of the *Dcr2* gene (Synthego). Guide RNA
573 was designed using CHOP-CHOP and verified using Cas-OFFinder to determine off-target effects
574 by searching the guide RNA sequence against the *Aedes albopictus* genome (JXUM01).
575 Synthesized sgRNA were also modified with 5' 2'-O-methyl (OMe) analogs and 3'
576 phosphorothioate (PS) to enhance stability and performance. We harvested $1X10^6$ cells two
577 weeks following Cas9-sgRNA transfection, extracted gDNA, and amplified the sgRNA target
578 region using flanking primers (Fwd: 5'-GACCCATATCGCCCTTATGGC-3', Rev: 5'-
579 TCGTAACTCCCAACGGTGGC-3'). Purified PCR products were sent for Sanger sequencing, and
580 the resulting chromatograms were used for TIDE analyses (version 5.0), which revealed a
581 knockout efficiency of 82-85% (Figure S2) (*66*).

582 *Ago2 silencing in U4.4 cells*

583 We used dsRNA to silence *Aedes albopictus Ago2* in U4.4 cells using previously described
584 methods (*39*). Briefly, total RNA extracted from U4.4 cells was used to generate cDNA using
585 oligo(dT). The cDNA was used as the template for PCR to amplify a region within the PIWI domain
586 of *Ago2* using primers carrying T7 promoters at the 5' end (Fwd: 5'-
587 TAATACGACTCACTATAGCATCGAGGGTTTCCGCTACA-3', Rev: 5'-
588 TAATACGACTCACTATAGGGTAATATGTCAGCGCCTGC-3'). Purified PCR products were used
589 as templates for *in vitro* transcription using T7 RNA polymerase (NEB) to generate double-
590 stranded RNA (dsRNA), which was then purified using the MEGAclear clean-up kit (Invitrogen)
591 according to the manufacturer's instructions. $5X10^5$ U4.4 cells were transfected with 500ng *Ago2*
592 dsRNA using Lipofectamine 3000 (Invitrogen) before assessing *Ago2* silencing over 1-4 days
593 using qRT-PCR (Fwd: 5'- ACTGGATAAGAAACGGGGCG-3', Rev: 5'-
594 TGCTTGGCGACGATGTTTTG-3'). To determine the extent of functional disruption of the siRNA
595 pathway following *Ago2* silencing, we used a previously described eGFP-reporter silencing assay
596 via dsRNA targeting eGFP (dsGFP) (Figure S5A). Infections were performed 48 hours post *Ago2*
597 dsRNA treatment.

598 *Small RNA sequencing and analysis*

599 10 µg of total RNA was isolated from cultured U4.4 and C6/36 mosquito cells five days following
600 infection with SINV. RNA purity and integrity were analyzed using Agilent 4200 TapeStation. All
601 subsequent small RNA enrichment steps were performed by Novogene, USA, using 10 µg of total

RNA. Small RNA sequencing was conducted using an Illumina Novaseq (Novogene, USA). Three biological replicate libraries were sequenced for each sample. After removing adaptor sequences (Trimmomatic), the processed reads were mapped to the SINV genome (strain TE12) using Geneious Mapper with a mapping quality set to 30, a 10% gap, and a 20% mismatch rate The standard counts-per-million (CPM) method ((CPM = gene read count/total mapped reads) × 1,000,000) was used to normalize for sequencing depth for comparing small RNA counts between samples. Logoplots showing nucleotide frequencies within vpiRNA reads were generated using 24-31nt vpiRNA reads and visualized using WebLogo 3 (*67*).

Virus Constructs

All viral stop-codon mutant plasmids were generated by site-directed mutagenesis. SINV sense-codon variants were generated in our previous study (*1*). SINV E1-hs_{mut} variant was generated using the following primer pair (Fwd: 5'-CTCGGAGAATTCACAAATGAGCGAGGCCTATGTCGAATTGTCAGCAGATTGCGCGT-3', Rev: 5'- TGTGAATTCTCCGAGTCGCAGAAGCATTGTGCTCCTCCCCACATAAAGGGGTAGAC-3'). Mutagenic primers were designed using Takara's In-Fusion Cloning Primer Design tool. PCR reactions were performed using Phusion polymerase (NEB) with the following cycling conditions: 1. 98°C for 30 sec, 2. 98°C for 30 sec, 3. 50°C for 30 sec, 4. 72°C for 7 min (Repeat steps 2-4 18x), 5. 72°C for 10 min, 6. Hold at 4°C. Reactions were then treated with *DpnI* for 6 hours and purified using the Monarch PCR and DNA Clean-up Kit (NEB) according to the manufacturer's protocol. The purified reaction was then transformed into DH5α cells, and DNA was isolated using the Monarch Plasmid Miniprep Kit (NEB) according to the manufacturer's protocol. Luciferase-based reporter viruses were generated by digesting parental and mutant plasmids with *SpeI* (NEB) and cloning in luciferase (Nano) using HiFi Gibson assembly (NEB). The Gibson reactions were then transformed into DH5α cells, and DNA was isolated using the Monarch Plasmid Miniprep Kit (NEB) according to the manufacturer's protocol.

Independent Viral Growth Assays

2 µg of infectious clones were linearized with *XhoI* (NEB) and subjected to *in vitro* transcription (IVT) using SP6 RNA polymerase (NEB) according to the manufacturer's suggested protocol. Cells were seeded into 24-well plates to achieve 70-80% confluency and transfected with IVTs using Lipofectamine LTX (Thermo Fisher) according to the manufacturer's protocol. Cells were collected 48 hours post-transfection and analyzed by flow cytometry (BD Fortessa). Infection rates of all variants were normalized relative to that of wild-type SINV (550opal).

Viral Competition Assays

Genome copies of WT and mutant virus stocks were calculated using quantitative RT-PCR. Briefly, cDNA synthesis was performed on the viral supernatant using M-MuLV Reverse Transcriptase (NEB) with oligo(dT) (20mer + 5'-Phos) (IDT) according to the manufacturer's protocol. RT-qPCR analysis was performed using SYBR Green master mix (Thermo Fisher) with gene-specific primers, according to the manufacturer's protocol, on the Applied Biosystems StepOnePlus Real-Time PCR System (Life Technologies). Once obtained, WT and mutant SINV virus stocks were normalized to equal genome copies. Wild-type and *Dcr2* KO U4.4 cells, and C6/36 cells were seeded into 24 wells and infected with TE3'2J-mCherry wild-type virus alongside TE3'2J: eGFP wild-type or mutant viruses at a 1:1 ratio (MOI – 0.1). Cells were collected 48 hours post-infection and analyzed by flow cytometry (BD Fortessa) to determine the percentage of cells infected with wild-type (red) and variant (green) viruses. The viral competitive index was calculated as the ratio of variant (eGFP) to wild-type (mCherry) infected cells within the population.

Generation of trans-heterozygous Dcr2 mutant mosquitoes

Dcr2 eGFP null line: We previously developed a transgenic line containing eGFP, as originally described in Basu et al. (*20*). Initially, we created an out-of-frame deletion using TALEN technology. Loss of function was confirmed using multiple approaches, including crossing into

our "sensor" line and observing disease phenotypes following challenge with both alphavirus and flavivirus pathogens (*21*, *68*). Using the same TALEN target site, we knocked in a construct containing eGFP under the control of the Poly-UB promoter, as described in Basu et al. (*20*).

Dcr2 dsRED null line: For insertion of the dsRED-containing construct, we employed sgRNA-directed Cas9 nuclease. The sgRNA was designed to target a site adjacent to the original TALEN location. We developed two distinct donor constructs featuring different homology arm sequences. Prior to creating these constructs, we sequenced the target site, which revealed polymorphisms within the intronic regions of the homology arms. To account for this genetic variation, we generated donor constructs based on the two most prevalent homology arm sequences identified across individual mosquito specimens. Both donor constructs were co-injected during the transformation procedure. We confirmed one insertion site junction, but the second junction remains unverified. However, confirming genomic insertions in *Ae. aegypti* presents significant technical challenges due to the genome's architecture and heterogeneity, particularly the presence of numerous large introns containing many repetitive sequences, and the previously mentioned polymorphisms.

Dcr2 homozygous knockouts: We generated trans-heterozygous *Dcr2*-/- mosquitoes by crossing the two distinct Dcr2 mutant lines, one expressing eGFP (whole body expression) and the other dsRED (whole body expression) (Figure 2A). The progeny from these crosses were screened at the larval stage for fluorescent marker expression.

In vivo mosquito infections

Adult *Aedes aegypti* mosquitoes were infected by injecting 0.5 µl of Sindbis virus (SINV; 10^6 $TCID_{50}$/ml) diluted in Dulbecco's Modified Eagle Medium (DMEM) directly into the thorax. Wild-type siblings, identified as negative for EGFP and dsRED fluorescence, were used as controls. Following inoculation, *Dcr2* null (*Dcr2* -/-) mutants and wild-type siblings were maintained at 28 °C and 80% relative humidity under a 14:10 h light: dark cycle. Mosquitoes were collected at 0 and 72 hours post-infection in pools of five, flash frozen in liquid nitrogen, and stored at −80 °C until further analysis. Quantitative RT-PCR (qRT-PCR) analysis was performed to determine viral RNA levels in total RNA extracted from pools of five mosquitoes per replicate. A separate set of individual mosquitoes (n = 15/condition) was collected and flash-frozen for quantification of infectious virus titer via $TCID_{50}$ assays on Vero cells. Mosquitoes were homogenized in 60 µL of sterile 1× PBS containing protease inhibitor and clarified by centrifugation through a 0.45µm Ultra-free PVDF filter. Survival curves of wild-type SINV (550opal) infected *Dcr2*+/+ and *Dcr2*-null mosquitoes were carried out over a period of 22 days with ≥28 female mosquitoes that were infected with 10^6 $TCID_{50}$/ml wild-type SINV.

Total RNA Extractions and Real-Time Quantitative RT-PCR Analysis

To quantify the copies of minus-strand and plus-strand RNA, cells were seeded into a 24-well plate and infected with WT or variants at greater than 90% confluency. At 4 and 18 hours post-infection, cells were harvested using TRIzol reagent (Thermo Fisher), and RNA was extracted using the Direct-zol RNA Miniprep kit (Zymo) according to the manufacturer's protocol. Following RNA extraction, cDNA was synthesized using M-MuLV Reverse Transcriptase (NEB) with strand-specific primers or OligoDT (20mer+5'Phos) (IDT) according to the manufacturer's protocol. In all cases, RT-qPCR analysis was performed using SYBR Green master mix (Thermo Fisher) with plus-strand-specific primers according to the manufacturer's protocol, and the Applied Biosystems StepOnePlus qRT-PCR machine (Life Technologies) was used.

Viral Replication Assays

SINV nsP3-Nluc reporter viruses were generated by digesting 2µg plasmid DNA with *XhoI* and performing in vitro transcription (IVT) using SP6 RNA polymerase (NEB) according to the manufacturer's protocol. Cells were seeded into black-walled, clear-bottom 96-well plates at 70-80% confluency and transfected with 100 ng of capped viral RNA using Lipofectamine LTX

700 (Thermo-Fisher) according to the manufacturer's protocol. At 48 hours post-transfection,
701 translation was quantified using the NanoGlo luciferase assay system (Promega) according to the
702 manufacturer's protocol. Luminescence was recorded using a Cytation3 Imaging Reader
703 (BioTek).

704 *IFN reporter activity*

705 To quantify levels of secreted IFN from infected wild-type, *MDA5* KO, and *MAVS* KO A549 cells,
706 cell supernatants from wild-type SINV (550opal) and 550C infected cells were harvested 16 hours
707 post-infection and transferred onto 5xISGF3-GLuc Huh7 reporter cells (*41*). Reporter cells were
708 then incubated at 37°C and 5% CO_2 for 48 hours to allow GLuc secretion into the media.
709 Secreted GLuc was quantified using the Pierce Gaussia Luciferase Assay kit (Thermo Fisher
710 Scientific) on a Cytation3 plate reader (BioTek) as per the manufacturer's protocol. The *MDA5*
711 KO A549 and 5XISGF3-GLuc Huh7 reporter cells were a gift from Dr. Ram Savan (University of
712 Washington). The *MAVS* KO A549 cells were a gift from Dr. Dan Stetson (University of
713 Washington).

714 *Western Blot Analyses*

715 Cells were seeded into six-well plates and infected at an MOI = 5. Cells were washed with cold
716 1X PBS, and lysates were harvested using RIPA buffer (Pierce) supplemented with 1X protease
717 inhibitor (cOmplete) after a 1-hour incubation at 4 °C. Purified protein was denatured using 2X
718 Laemmli buffer (BioRad) with 5% β-Mercaptoethanol (Sigma-Aldrich). Western blots were run on
719 Mini-PROTEAN precast gels and then transferred to a Trans-Blot 0.2 µm nitrocellulose membrane
720 using the Trans-Blot Turbo Transfer System (Bio-Rad). Blots were incubated overnight at 4 °C in
721 5% BSA and primary antibody at a 1:3,000 dilution, then washed with 1X TBS containing 0.1%
722 Tween-20. The blots were then probed with a secondary α-rabbit HRP-conjugate (R&D Systems).
723 Blots were visualized using a Bio-Rad ChemiDoc Imaging System. Western blots probing for non-
724 structural protein expression and polyprotein processing were performed with independent
725 biological replicates for each virus under different host conditions.

726 *Immunofluorescence Confocal Microscopy*

727 Glass-bottom #1.5 coverslip 12-well plates (NC0190134; Thermo Fisher Scientific) were treated
728 with 200 µl of sterile 0.01% poly-L-lysine for cell culture (P4832; Sigma-Aldrich) per well for 1 hour
729 at room temperature, rinsed once with DPBS++ (14-040-216; Thermo Fisher Scientific), and
730 allowed to dry for 1 hour. U4.4 cells were seeded onto poly-L-lysine-coated wells and grown to
731 approximately 20% confluency before infection with wild-type (WT) or 550C SINV 3XF-GFP at
732 high multiplicity of infection (MOI) for 48 hours. Cells were rinsed twice with DPBS++ and then
733 fixed with 200 µl of 4% (v/v) paraformaldehyde (28906; Thermo Fisher Scientific) in DPBS++ for
734 10 minutes, followed by two washes. Permeabilization was performed using 400 µL of 0.05%
735 Triton X-100 (BP151; Thermo Fisher Scientific) in DPBS++ for 5 minutes, followed by two washes.
736 Cells were then blocked with 400 µl of 10% (w/v) bovine serum albumin (BSA; BP9703100;
737 Thermo Fisher Scientific) in DPBS++ for 1 hour.

738 The following steps were carried out in the dark to minimize photobleaching. Primary antibody
739 staining was performed using 500 µl of mouse monoclonal anti-dsRNA J2 (1:1000) (76651L; Cell
740 Signaling) in 5% BSA, incubated overnight at 4°C with gentle agitation. Cells were washed three
741 times with DPBS++ and blocked again with 400 µl of 10% BSA in DPBS++ for 1 hour. Secondary
742 antibody staining was performed using 500 µl of Alexa Fluor 633-conjugated goat anti-mouse
743 antibody (1:1000) (A-21050; Invitrogen) in 5% BSA, incubated overnight at 4°C without agitation.
744 After washing once with DPBS++, the nuclei were counterstained with Hoechst 33258 (1:1000)
745 (H1398; Invitrogen) in 5% BSA for 15 minutes and then washed three times. Coverslips were
746 mounted using 150 µl of SlowFade™ Diamond Antifade Mountant (S36972; Thermo Fisher
747 Scientific). All steps were carried out at room temperature unless otherwise noted. Each wash
748 used DPBS++ for 5 minutes. Imaging was performed using a Leica STELLARIS confocal
749 microscope (DMi8 stand) with a 63x oil-immersion objective and Leica Application Suite X (LAS

X) software. All compared microscopy images were acquired on the same day with the same microscopy settings.

Microscopy Imaging Analysis

Images were analyzed using FIJI/ImageJ 1.54f with Java 1.8.0_322 (64-bit) and the ImageJ 3D Suite MCIB V3.96 (*69–71*). Spherule boundaries were determined via MaxEntropy thresholding of anti-dsRNA Alexa Fluor 633 signal and used to create 3D regions of interest (ROIs). The accessibility of spherules to cytoplasmic eGFP was determined by quantifying the mean eGFP signal intensity in entire spherules using the 3D Manager Quantif3D function in the ImageJ 3D Suite plugin. Spherule boundaries (Figure S12D) were determined via MaxEntropy thresholding of anti-dsRNA Alexa Fluor 633 signal and used to create 3D regions of interest (ROIs). Reported mean eGFP signal intensities are per-spherule. Cellular dsRNA levels were determined by quantifying the mean anti-dsRNA Alexa Fluor 633 signal using the 3D Manager Quantif3D function in the ImageJ 3D Suite plugin. Infected cells were identified by cytoplasmic eGFP expression and the presence of spherules. Cellular boundaries were determined via Otsu thresholding of cytoplasmic eGFP signal, and areas excluding eGFP were included using the binary 'Fill in Holes' function, creating 3D ROIs as defined by the 3D Object Counter with a minimum threshold of 1,500 cubic voxels. If needed, neighboring cells were separated across the entire stack before quantification using the 3D Watershed function in the ImageJ 3D Suite plugin. Nuclei were used as seeds. Reported mean J2 signal intensities are on a per-cell basis.

Phylogenetics and RNA Structure Analysis

A multiple sequence alignment of nsP4 coding sequences from 49 extant alphavirus species was constructed using Clustal Omega. Alignments were manually curated in Geneious, and maximum-likelihood phylogenetic trees were generated using the HKY85 substitution model in PHYML with 100 bootstrap replicates for statistical support. The phylogenetic tree was visualized using FigTree. RNA secondary structure conservation was determined using RNAalifold, which was performed on a multiple sequence alignment of the 45-nt-long E1-hs region from 2,086 alphavirus sequences collected from BV-BRC (v3.51.7) (*72*). SHAPE-constrained RNA secondary structure was generated using Vienna RNAfold with SHAPE-MaP data previously generated by *Kutchko et al.* (*30*).

Statistics

Statistical analyses were conducted using GraphPad Prism (v10.2, GraphPad Software Inc., San Diego, CA). Data were first checked for normality (Gaussian distribution) using the Kolmogorov-Smirnov test. For data meeting normality ($\alpha = 0.05$) and homogeneity of variance criteria, means were compared using, unless otherwise stated, a Two-Way ANOVA (for multiple groups with two variables), with post hoc tests used for multiple comparisons. To determine the genetic relationship between viral mutations, we employed a modified Combination Index (CI) analysis based on the Chou-Talalay method to quantify combinatorial effects (*73*).

Acknowledgments

We thank the members of the Malik and Emerman labs for their valuable discussions and acknowledge Megan Levy, Peter Dietzen, and Rebecca Fereira Alves for providing valuable feedback on the manuscript. We thank Richard W. Hardy and Suchetana (Tuli) Mukhopadhyay (Indiana University Bloomington) for sharing critical reagents, including the parental SINV infectious clone plasmids and E1/E2 polyclonal serum. We are thankful to Dr. Ram Savan (University of Washington) for sharing *MDA5* KO A549 and 5XISGF3-GLuc Huh7 reporter cells, and Dr. Dan Stetson (University of Washington) for sharing *MAVS* KO A549 cells. We thank the Hutch Shared Resources, especially the Genomics and Flow Cytometry Core Facilities, for providing technical support.

Funding:

Shared resources grant support
Helen Hay Whitney Fellowship (to TB)
National Institutes of Health grant U54 AI170792 (PI: Nevan Krogan) (to ME, HSM)
National Institutes of Health grant AI141532 (to KMM)
Howard Hughes Medical Institute Investigator Award (to HSM).
Funding agencies had no role in the execution of the project or in the decision to publish.

Author contributions:

Conceptualization: TB, TSF, EMA, HSM
Methodology: TB, TSF, EMA, FW, KM, LC, HSM
Investigation: TB, TSF, EMA, FW, LC
Formal Analysis: TB, TSF, EMA
Validation: TB, TSF, EMA
Visualization: TB, TSF, HSM
Resources: TB, TSF, KM, HSM
Data curation: TB, TSF, KM, HSM
Funding acquisition: TB, ME, KM, HSM
Project administration: TB, KM, HSM
Supervision: TB, ME, KM, HSM
Writing – original draft: TB, TSF, HSM
Writing – review & editing: TB, TSF, EMA, ME, KM, HSM

Competing Interests: The authors declare they have no competing interests.

Data and Materials Availability: All data needed to evaluate the conclusions in the paper are present in the paper and/or the Supplementary Materials.

List of Supplementary Materials: Figures S1-S12

References

1. T. Bhattacharya, E. M. Alleman, T. S. Freeman, A. C. Noyola, M. Emerman, H. S. Malik, A conserved opal termination codon optimizes a temperature-dependent trade-off between protein production and processing in alphaviruses. *Science Advances* **11**, eads7933 (2025).

2. J. C. Rupp, K. J. Sokoloski, N. N. Gebhart, R. W. Hardy, Alphavirus RNA synthesis and non-structural protein functions. *Journal of General Virology* **96**, 2483–2500 (2015).

3. G. P. Li, C. M. Rice, Mutagenesis of the in-frame opal termination codon preceding nsP4 of Sindbis virus: studies of translational readthrough and its effect on virus replication. *J Virol* **63**, 1326–1337 (1989).

4. K. M. Myles, C. L. H. Kelly, J. P. Ledermann, A. M. Powers, Effects of an Opal Termination Codon Preceding the nsP4 Gene Sequence in the O'Nyong-Nyong Virus Genome on *Anopheles gambiae* Infectivity. *J Virol* **80**, 4992–4997 (2006).

5. J. E. Jones, K. M. Long, A. C. Whitmore, W. Sanders, L. R. Thurlow, J. A. Brown, C. R. Morrison, H. Vincent, K. M. Peck, C. Browning, N. Moorman, J. K. Lim, M. T. Heise, Disruption of the Opal Stop Codon Attenuates Chikungunya Virus-Induced Arthritis and Pathology. *mBio* **8**, e01456-17 (2017).

6. B. C. Mounce, T. Cesaro, L. Vlajnić, A. Vidiņa, T. Vallet, J. Weger-Lucarelli, G. Passoni, K. A. Stapleford, J.-P. Levraud, M. Vignuzzi, Chikungunya Virus Overcomes Polyamine Depletion

840 by Mutation of nsP1 and the Opal Stop Codon To Confer Enhanced Replication and Fitness.
841 *J Virol* **91**, e00344-17 (2017).

842 7. R. Li, K. Sun, A. Tuplin, M. Harris, A structural and functional analysis of opal stop codon
843 translational readthrough during Chikungunya Virus replication. bioRxiv [Preprint] (2023).
844 https://doi.org/10.1101/2023.07.24.550286.

845 8. K. Hwang Kim, T. Rümenapf, E. G. Strauss, J. H. Strauss, Regulation of Semliki Forest virus
846 RNA replication: a model for the control of alphavirus pathogenesis in invertebrate hosts.
847 *Virology* **323**, 153–163 (2004).

848 9. S. C. Weaver, A. C. Brault, W. Kang, J. J. Holland, Genetic and Fitness Changes
849 Accompanying Adaptation of an Arbovirus to Vertebrate and Invertebrate Cells. *J Virol* **73**,
850 4316–4326 (1999).

851 10. F. Nasar, G. Palacios, R. V. Gorchakov, H. Guzman, A. P. T. Da Rosa, N. Savji, V. L. Popov,
852 M. B. Sherman, W. I. Lipkin, R. B. Tesh, S. C. Weaver, Eilat virus, a unique alphavirus with
853 host range restricted to insects by RNA replication. *Proc Natl Acad Sci U S A* **109**, 14622–
854 14627 (2012).

855 11. K. Hermanns, M. Marklewitz, F. Zirkel, G. J. Overheul, R. A. Page, J. R. Loaiza, C. Drosten, R.
856 P. van Rij, S. Junglen, Agua Salud alphavirus defines a novel lineage of insect-specific
857 alphaviruses discovered in the New World. *J Gen Virol* **101**, 96–104 (2020).

858 12. K. Hermanns, F. Zirkel, A. Kopp, M. Marklewitz, I. B. Rwego, A. Estrada, T. R. Gillespie, C.
859 Drosten, S. Junglen, Discovery of a novel alphavirus related to Eilat virus. *J Gen Virol* **98**,
860 43–49 (2017).

861 13. K. M. Myles, M. R. Wiley, E. M. Morazzani, Z. N. Adelman, Alphavirus-derived small RNAs
862 modulate pathogenesis in disease vector mosquitoes. *Proceedings of the National Academy*
863 *of Sciences* **105**, 19938–19943 (2008).

864 14. M. Altinli, M. Leggewie, M. Badusche, R. Gyanwali, C. Scherer, J. Schulze, V. B. Sreenu, M.
865 Fegebank, B. Zibrat, J. Fuss, S. Junglen, E. Schnettler, Antiviral RNAi Response against the
866 Insect-Specific Agua Salud Alphavirus. *mSphere* **7**, e01003-21 (2022).

867 15. R. W. C. Siu, R. Fragkoudis, P. Simmonds, C. L. Donald, M. E. Chase-Topping, G. Barry, G.
868 Attarzadeh-Yazdi, J. Rodriguez-Andres, A. A. Nash, A. Merits, J. K. Fazakerley, A. Kohl,
869 Antiviral RNA Interference Responses Induced by Semliki Forest Virus Infection of Mosquito
870 Cells: Characterization, Origin, and Frequency-Dependent Functions of Virus-Derived Small
871 Interfering RNAs. *J Virol* **85**, 2907–2917 (2011).

872 16. L. R. Sabin, Q. Zheng, P. Thekkat, J. Yang, G. J. Hannon, B. D. Gregory, M. Tudor, S. Cherry,
873 Dicer-2 Processes Diverse Viral RNA Species. *PLOS ONE* **8**, e55458 (2013).

874 17. R. J. Gestuveo, R. Parry, L. B. Dickson, S. Lequime, V. B. Sreenu, M. J. Arnold, A. A.
875 Khromykh, E. Schnettler, L. Lambrechts, M. Varjak, A. Kohl, Mutational analysis of Aedes
876 aegypti Dicer 2 provides insights into the biogenesis of antiviral exogenous small interfering
877 RNAs. *PLOS Pathogens* **18**, e1010202 (2022).

878 18. D. E. Brackney, J. C. Scott, F. Sagawa, J. E. Woodward, N. A. Miller, F. D. Schilkey, J. Mudge,
879 J. Wilusz, K. E. Olson, C. D. Blair, G. D. Ebel, C6/36 Aedes albopictus Cells Have a
880 Dysfunctional Antiviral RNA Interference Response. *PLoS Negl Trop Dis* **4**, e856 (2010).

881 19. D. A. Simpson, N. L. Davis, S.-C. Lin, D. Russell, R. E. Johnston, Complete Nucleotide
882 Sequence and Full-Length cDNA Clone of S.A.AR86, a South African Alphavirus Related to
883 Sindbis. *Virology* **222**, 464–469 (1996).

884 20. S. Basu, A. Aryan, J. M. Overcash, G. H. Samuel, M. A. E. Anderson, T. J. Dahlem, K. M.
885 Myles, Z. N. Adelman, Silencing of end-joining repair for efficient site-specific gene insertion
886 after TALEN/CRISPR mutagenesis in Aedes aegypti. *Proceedings of the National Academy*
887 *of Sciences* **112**, 4038–4043 (2015).

888 21. G. H. Samuel, T. Pohlenz, Y. Dong, N. Coskun, Z. N. Adelman, G. Dimopoulos, K. M. Myles,
889 RNA interference is essential to modulating the pathogenesis of mosquito-borne viruses in
890 the yellow fever mosquito Aedes aegypti. *Proceedings of the National Academy of Sciences*
891 **120**, e2213701120 (2023).

892 22. E. M. Morazzani, M. R. Wiley, M. G. Murreddu, Z. N. Adelman, K. M. Myles, Production of
893 Virus-Derived Ping-Pong-Dependent piRNA-like Small RNAs in the Mosquito Soma. *PLOS*
894 *Pathogens* **8**, e1002470 (2012).

895 23. P. Miesen, E. Girardi, R. P. van Rij, Distinct sets of PIWI proteins produce arbovirus and
896 transposon-derived piRNAs in Aedes aegypti mosquito cells. *Nucleic Acids Res* **43**, 6545–
897 6556 (2015).

898 24. P. Miesen, J. Joosten, R. P. van Rij, PIWIs Go Viral: Arbovirus-Derived piRNAs in Vector
899 Mosquitoes. *PLOS Pathogens* **12**, e1006017 (2016).

900 25. M. Varjak, K. Maringer, M. Watson, V. B. Sreenu, A. C. Fredericks, E. Pondeville, C. L. Donald,
901 J. Sterk, J. Kean, M. Vazeille, A.-B. Failloux, A. Kohl, E. Schnettler, Aedes aegypti Piwi4 Is a
902 Noncanonical PIWI Protein Involved in Antiviral Responses. *mSphere* **2**, e00144-17 (2017).

903 26. N. Vodovar, A. W. Bronkhorst, K. W. R. Van Cleef, P. Miesen, H. Blanc, R. P. Van Rij, M.-C.
904 Saleh, Arbovirus-Derived piRNAs Exhibit a Ping-Pong Signature in Mosquito Cells. *PLoS*
905 *ONE* **7**, e30861 (2012).

906 27. Y. Luo, P. He, N. Kanrar, K. Fejes Toth, A. A. Aravin, Maternally inherited siRNAs initiate piRNA
907 cluster formation. *Molecular Cell* **83**, 3835-3851.e7 (2023).

908 28. E. Schnettler, C. L. Donald, S. Human, M. Watson, R. W. C. Siu, M. McFarlane, J. K.
909 Fazakerley, A. Kohl, R. Fragkoudis, Knockdown of piRNA pathway proteins results in
910 enhanced Semliki Forest virus production in mosquito cells. *J Gen Virol* **94**, 1680–1689
911 (2013).

912 29. J. L. Hyde, R. Chen, D. W. Trobaugh, M. S. Diamond, S. C. Weaver, W. B. Klimstra, J. Wilusz,
913 The 5′ and 3′ ends of alphavirus RNAs – Non-coding is not non-functional. *Virus Research*
914 **206**, 99–107 (2015).

915 30. K. M. Kutchko, E. A. Madden, C. Morrison, K. S. Plante, W. Sanders, H. A. Vincent, M. C.
916 Cruz Cisneros, K. M. Long, N. J. Moorman, M. T. Heise, A. Laederach, Structural divergence
917 creates new functional features in alphavirus genomes. *Nucleic Acids Research* **46**, 3657–
918 3670 (2018).

919 31. E. A. Madden, K. S. Plante, C. R. Morrison, K. M. Kutchko, W. Sanders, K. M. Long, S. Taft-
920 Benz, M. C. Cruz Cisneros, A. M. White, S. Sarkar, G. Reynolds, H. A. Vincent, A. Laederach,
921 N. J. Moorman, M. T. Heise, Using SHAPE-MaP To Model RNA Secondary Structure and

Identify 3′UTR Variation in Chikungunya Virus. *Journal of Virology* **94**, 10.1128/jvi.00701-20 (2020).

32. C. Bou-Nader, K. M. Juma, A. Bothra, A. J. Brasington, R. Ghirlando, M. Suzuki, D. N. Garboczi, S. H. Leppla, J. Zhang, Specificity and mechanism of the double-stranded RNA-specific J2 monoclonal antibody. bioRxiv [Preprint] (2025). https://doi.org/10.1101/2025.05.09.649859.

33. M. Bonin, J. OBERSTRAß, N. Lukacs, K. Ewert, E. Oesterschulze, R. Kassing, W. Nellen, Determination of preferential binding sites for anti-dsRNA antibodies on double-stranded RNA by scanning force microscopy. *RNA* **6**, 563–570 (2000).

34. T. Laurent, P. Kumar, S. Liese, F. Zare, M. Jonasson, A. Carlson, L.-A. Carlson, Architecture of the chikungunya virus replication organelle. *eLife* **11**, e83042 (2022).

35. K. Hellström, K. Kallio, A. Utt, T. Quirin, E. Jokitalo, A. Merits, T. Ahola, Partially Uncleaved Alphavirus Replicase Forms Spherule Structures in the Presence and Absence of RNA Template. *J Virol* **91**, e00787-17 (2017).

36. E. I. Frolova, R. Gorchakov, L. Pereboeva, S. Atasheva, I. Frolov, Functional Sindbis Virus Replicative Complexes Are Formed at the Plasma Membrane. *Journal of Virology* **84**, 11679–11695 (2010).

37. T. Ahola, G. McInerney, A. Merits, Alphavirus RNA replication in vertebrate cells. *Adv Virus Res* **111**, 111–156 (2021).

38. J. Liu, L. Swevers, A. Kolliopoulou, G. Smagghe, Arboviruses and the Challenge to Establish Systemic and Persistent Infections in Competent Mosquito Vectors: The Interaction With the RNAi Mechanism. *Front. Physiol.* **10** (2019).

39. I. Sánchez-Vargas, J. C. Scott, B. K. Poole-Smith, A. W. E. Franz, V. Barbosa-Solomieu, J. Wilusz, K. E. Olson, C. D. Blair, Dengue Virus Type 2 Infections of Aedes aegypti Are Modulated by the Mosquito's RNA Interference Pathway. *PLoS Pathog* **5**, e1000299 (2009).

40. P. V. Maillard, A. G. van der Veen, E. Z. Poirier, C. Reis e Sousa, Slicing and dicing viruses: antiviral RNA interference in mammals. *The EMBO Journal* **38**, e100941 (2019).

41. J. R. Smith, J. W. Dowling, M. I. McFadden, A. Karp, J. Schwerk, J. J. Woodward, R. Savan, A. Forero, MEF2A suppresses stress responses that trigger DDX41-dependent IFN production. *Cell Rep* **42**, 112805 (2023).

42. A. Chitrakar, S. Rath, J. Donovan, K. Demarest, Y. Li, R. R. Sridhar, S. R. Weiss, S. V. Kotenko, N. S. Wingreen, A. Korennykh, Real-time 2-5A kinetics suggest that interferons β and λ evade global arrest of translation by RNase L. *Proceedings of the National Academy of Sciences* **116**, 2103–2111 (2019).

43. I. Akhrymuk, I. Frolov, E. I. Frolova, Both RIG-I and MDA5 detect alphavirus replication in concentration-dependent mode. *Virology* **487**, 230–241 (2016).

44. V. Kril, M. Hons, C. Amadori, C. Zimberger, L. Couture, Y. Bouery, J. Burlaud-Gaillard, A. Karpov, D. Ptchelkine, A. L. Thienel, B. M. Kümmerer, A. Desfosses, R. Jones, P. Roingeard, L. Meertens, A. Amara, J. Reguera, Alphavirus nsP3 organizes into tubular scaffolds essential for infection and the cytoplasmic granule architecture. *Nat Commun* **15**, 8106 (2024).

963 45. Y. B. Tan, D. Chmielewski, M. C. Y. Law, K. Zhang, Y. He, M. Chen, J. Jin, D. Luo, Molecular
964 architecture of the Chikungunya virus replication complex. *Science Advances* **8**, eadd2536
965 (2022).

966 46. J. Girard, O. Le Bihan, J. Lai-Kee-Him, M. Girleanu, E. Bernard, C. Castellarin, M. Chee, A.
967 Neyret, D. Spehner, X. Holy, A.-L. Favier, L. Briant, P. Bron, In situ fate of Chikungunya virus
968 replication organelles. *Journal of Virology* **98**, e00368-24 (2024).

969 47. Y. Liu, J. Wang, Y. Han, X. Xia, R. Zeng, X. Fan, B. Zhang, K. Wang, J. Lei, Cryo-EM reveals
970 a double oligomeric ring scaffold of the CHIKV nsP3 peptide in complex with the NTF2L
971 domain of host G3BP1. *mBio* **16**, e03967-24.

972 48. G. Shin, S. A. Yost, M. T. Miller, E. J. Elrod, A. Grakoui, J. Marcotrigiano, Structural and
973 functional insights into alphavirus polyprotein processing and pathogenesis. *Proc. Natl.*
974 *Acad. Sci. U.S.A.* **109**, 16534–16539 (2012).

975 49. K. Bartholomeeusen, A. Utt, S. Coppens, K. Rausalu, K. Vereecken, K. K. Ariën, A. Merits, A
976 Chikungunya Virus trans-Replicase System Reveals the Importance of Delayed
977 Nonstructural Polyprotein Processing for Efficient Replication Complex Formation in
978 Mosquito Cells. *J Virol* **92**, e00152-18 (2018).

979 50. S. L. Moon, B. J. T. Dodd, D. E. Brackney, C. J. Wilusz, G. D. Ebel, J. Wilusz, Flavivirus sfRNA
980 suppresses antiviral RNA interference in cultured cells and mosquitoes and directly interacts
981 with the RNAi machinery. *Virology* **485**, 322–329 (2015).

982 51. K. W. R. van Cleef, J. T. van Mierlo, P. Miesen, G. J. Overheul, J. J. Fros, S. Schuster, M.
983 Marklewitz, G. P. Pijlman, S. Junglen, R. P. van Rij, Mosquito and Drosophila
984 entomobirnaviruses suppress dsRNA- and siRNA-induced RNAi. *Nucleic Acids Research*
985 **42**, 8732–8744 (2014).

986 52. R. Aliyari, Q. Wu, H.-W. Li, X.-H. Wang, F. Li, L. D. Green, C. S. Han, W.-X. Li, S.-W. Ding,
987 Mechanism of induction and suppression of antiviral immunity directed by virus-derived
988 small RNAs in Drosophila. *Cell Host Microbe* **4**, 387–397 (2008).

989 53. J. A. Chao, J. H. Lee, B. R. Chapados, E. W. Debler, A. Schneemann, J. R. Williamson, Dual
990 modes of RNA-silencing suppression by Flock House virus protein B2. *Nat Struct Mol Biol*
991 **12**, 952–957 (2005).

992 54. Q. Qian, H. Zhou, T. Shu, J. Mu, Y. Fang, J. Xu, T. Li, J. Kong, Y. Qiu, X. Zhou, The Capsid
993 Protein of Semliki Forest Virus Antagonizes RNA Interference in Mammalian Cells. *J Virol* **94**,
994 e01233-19 (2020).

995 55. K. Mathur, A. Anand, S. K. Dubey, N. Sanan-Mishra, R. K. Bhatnagar, S. Sunil, Analysis of
996 chikungunya virus proteins reveals that non-structural proteins nsP2 and nsP3 exhibit RNA
997 interference (RNAi) suppressor activity. *Sci Rep* **6**, 38065 (2016).

998 56. C. M. Cirimotich, J. C. Scott, A. T. Phillips, B. J. Geiss, K. E. Olson, Suppression of RNA
999 interference increases alphavirus replication and virus-associated mortality in Aedes aegypti
1000 mosquitoes. *BMC Microbiol* **9**, 49 (2009).

1001 57. C. C. Cruz, M. S. Suthar, S. A. Montgomery, R. Shabman, J. Simmons, R. E. Johnston, T. E.
1002 Morrison, M. T. Heise, Modulation of type I IFN induction by a virulence determinant within
1003 the alphavirus nsP1 protein. *Virology* **399**, 1–10 (2010).

1004 58. X. Liu, M. Mutso, A. Utt, A. Lepland, L. J. Herrero, A. Taylor, J. Bettadapura, P. A. Rudd, A.
1005 Merits, S. Mahalingam, Decreased Virulence of Ross River Virus Harboring a Mutation in the
1006 First Cleavage Site of Nonstructural Polyprotein Is Caused by a Novel Mechanism Leading
1007 to Increased Production of Interferon-Inducing RNAs. *mBio* **9**, 10.1128/mbio.00044-18
1008 (2018).

1009 59. N. Vasilakis, E. R. Deardorff, J. L. Kenney, S. L. Rossi, K. A. Hanley, S. C. Weaver, Mosquitoes
1010 Put the Brake on Arbovirus Evolution: Experimental Evolution Reveals Slower Mutation
1011 Accumulation in Mosquito Than Vertebrate Cells. *PLOS Pathogens* **5**, e1000467 (2009).

1012 60. A. T. Ciota, L. D. Kramer, Insights into Arbovirus Evolution and Adaptation from Experimental
1013 Studies. *Viruses* **2**, 2594–2617 (2010).

1014 61. B. M. Althouse, K. A. Hanley, The tortoise or the hare? Impacts of within-host dynamics on
1015 transmission success of arthropod-borne viruses. *Philosophical Transactions of the Royal*
1016 *Society B: Biological Sciences* **370**, 20140299 (2015).

1017 62. L. L. Coffey, N. Vasilakis, A. C. Brault, A. M. Powers, F. Tripet, S. C. Weaver, Arbovirus
1018 evolution in vivo is constrained by host alternation. *Proceedings of the National Academy of*
1019 *Sciences* **105**, 6970–6975 (2008).

1020 63. S. Bera, A. Fraile, F. García-Arenal, Analysis of Fitness Trade-Offs in the Host Range
1021 Expansion of an RNA Virus, Tobacco Mild Green Mosaic Virus. *Journal of Virology* **92**,
1022 10.1128/jvi.01268-18 (2018).

1023 64. X. 'May' Wang, J. Muller, M. McDowell, D. A. Rasmussen, Quantifying the strength of viral
1024 fitness trade-offs between hosts: a meta-analysis of pleiotropic fitness effects. *Evolution*
1025 *Letters*, qrae038 (2024).

1026 65. D. H. Goldhill, P. E. Turner, The evolution of life history trade-offs in viruses. *Current Opinion*
1027 *in Virology* **8**, 79–84 (2014).

1028 66. E. K. Brinkman, T. Chen, M. Amendola, B. van Steensel, Easy quantitative assessment of
1029 genome editing by sequence trace decomposition. *Nucleic Acids Research* **42**, e168 (2014).

1030 67. G. E. Crooks, G. Hon, J.-M. Chandonia, S. E. Brenner, WebLogo: a sequence logo generator.
1031 *Genome Res* **14**, 1188–1190 (2004).

1032 68. Z. N. Adelman, M. A. E. Anderson, E. M. Morazzani, K. M. Myles, A transgenic sensor strain
1033 for monitoring the RNAi pathway in the yellow fever mosquito, *Aedes aegypti*. *Insect*
1034 *Biochemistry and Molecular Biology* **38**, 705–713 (2008).

1035 69. J. Ollion, J. Cochennec, F. Loll, C. Escudé, T. Boudier, TANGO: a generic tool for high-
1036 throughput 3D image analysis for studying nuclear organization. *Bioinformatics* **29**, 1840–
1037 1841 (2013).

1038 70. J. Schindelin, I. Arganda-Carreras, E. Frise, V. Kaynig, M. Longair, T. Pietzsch, S. Preibisch,
1039 C. Rueden, S. Saalfeld, B. Schmid, J.-Y. Tinevez, D. J. White, V. Hartenstein, K. Eliceiri, P.
1040 Tomancak, A. Cardona, Fiji: an open-source platform for biological-image analysis. *Nat*
1041 *Methods* **9**, 676–682 (2012).

1042 71. A. B. Schroeder, E. T. A. Dobson, C. T. Rueden, P. Tomancak, F. Jug, K. W. Eliceiri, The
1043 ImageJ ecosystem: Open-source software for image visualization, processing, and analysis.
1044 *Protein Science* **30**, 234–249 (2021).

1045 72. S. H. Bernhart, I. L. Hofacker, S. Will, A. R. Gruber, P. F. Stadler, RNAalifold: improved
1046 consensus structure prediction for RNA alignments. *BMC Bioinformatics* **9**, 474 (2008).

1047 73. T. C. Chou, P. Talalay, Quantitative analysis of dose-effect relationships: the combined effects
1048 of multiple drugs or enzyme inhibitors. *Adv Enzyme Regul* **22**, 27–55 (1984).

1049

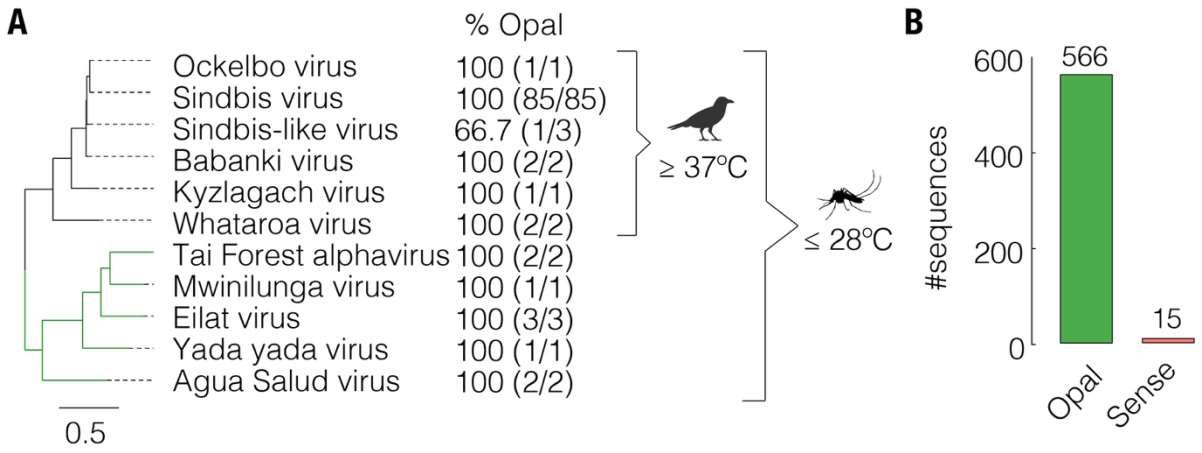

Fig. S1. Conservation of the nsP3 opal stop codon among mosquito-isolated alphaviruses. (A) A maximum-likelihood phylogenetic tree of two closely related dual-host and insect-specific alphavirus clades was constructed from whole-genome sequences. The percent occurrence of the nsP3 opal codon shown next to each taxon was calculated based on publicly available sequences. Note, however, that except for Sindbis virus, which has 85 reported sequences, there are only a few sequences available (shown in parentheses) for each of the other viruses. (B) Percent occurrence of the nsP3 opal codon and the extended PRT codon context UGAC among all available mosquito-isolated alphavirus sequences (n = 581). Numbers above each bar indicate the number of analyzed sequences.

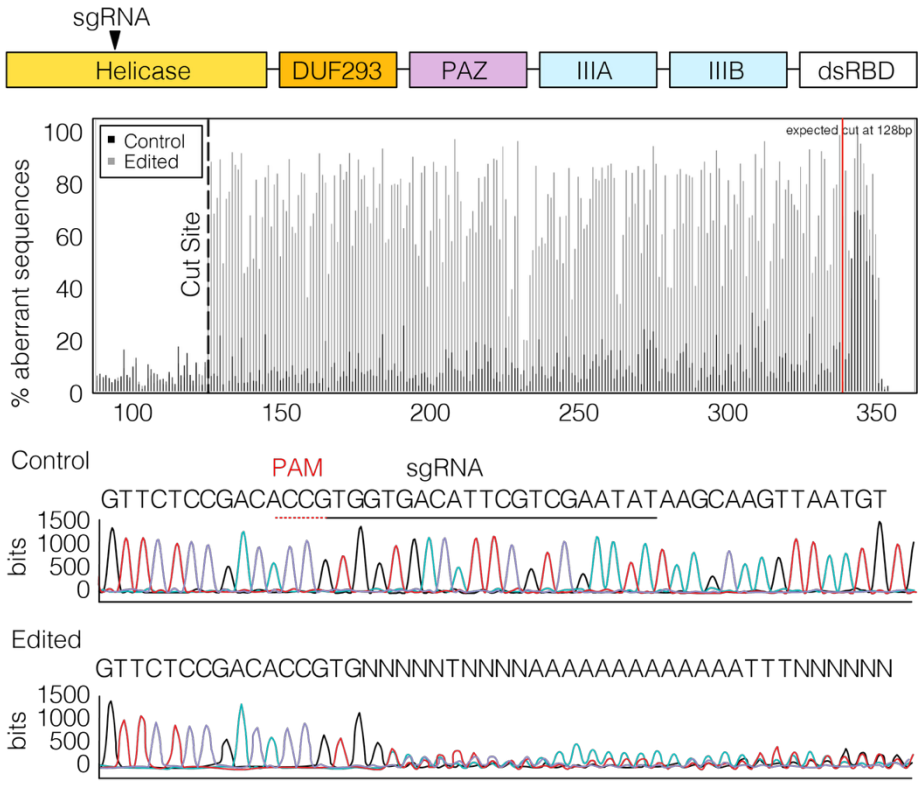

Fig. S2. Editing efficiency of *Dcr2* KO U4.4 cells. Domain structure of *Aedes* Dicer 2 protein. The black arrow indicates the approximate location of the CRISPR sgRNA target. (Middle) TIDE analysis plot showing editing efficiency in U4.4 cells. The vertical dashed line represents the expected cut site. (Bottom) Chromatogram of the *Dcr-2* target region in control and CRISPR-edited cells. The region past the vertical red line shows a drop in sequence quality.

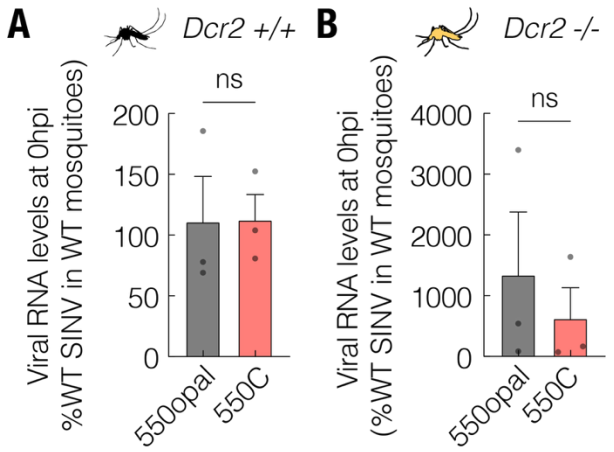

Fig. S3. Initial viral inoculum levels among injected mosquitoes. (A) Wild-type (*Dcr2* +/+) and (B) *Dcr2* KO (*Dcr2* -/-) *Aedes aegypti* mosquitoes were infected with SINV 550opal and 550C. Approximately 0-2 h after infection, injected mosquitoes were collected, and viral RNA was quantified by qRT-PCR. Data represent three independent biological replicates, each consisting of five pooled mosquitoes. Error bars represent the standard error of the mean (SEM). Unpaired t-test. ns = not significant.

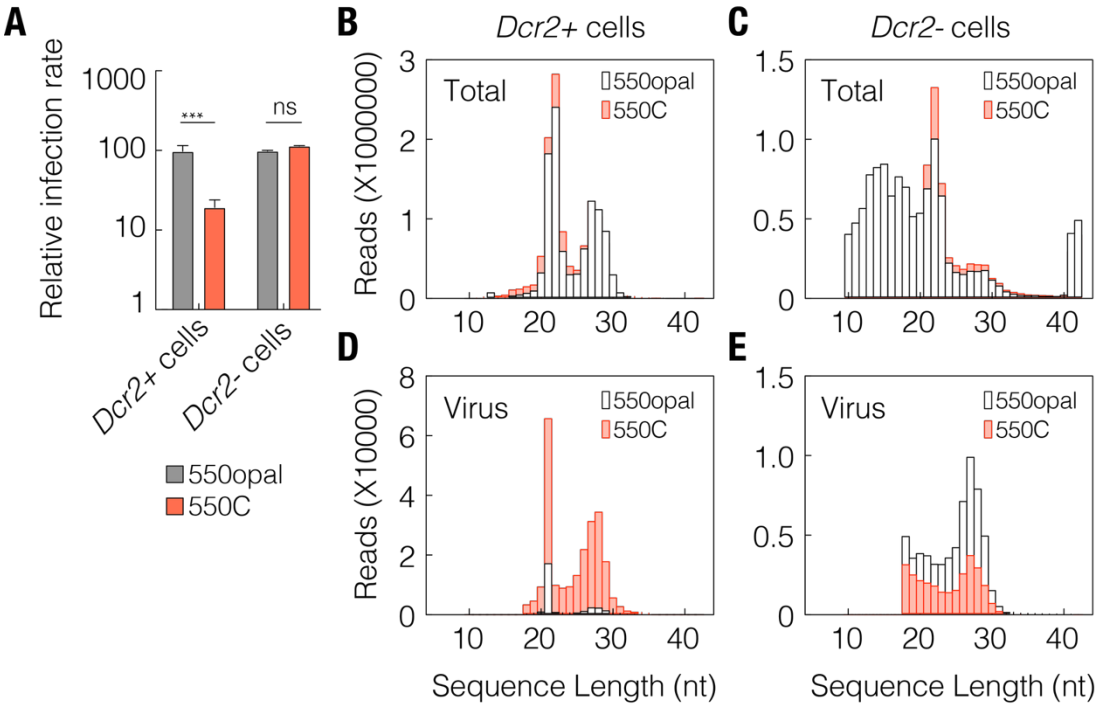

Fig. S4. Small RNA read distribution in *Dcr2*+ U4.4 and *Dcr2*- C6/36 cells. (A) Relative infection rates of SINV 550opal and 550C in *Dcr2*+ and *Dcr2*- cells used for Small RNAseq. (B-C) Total read counts of small RNA isolated from *Dcr2*+ (B) and *Dcr2*- (C) cells infected with wild-type SINV 550opal and SINV 550C. (D-E) Virus-specific read counts of small RNA isolated from *Dcr2*+ (D) and *Dcr2*- (E) cells infected with wild-type SINV 550opal and SINV 550C. The data represent three independent biological replicates. Error bars represent the standard error of the mean (SEM). Two-way ANOVA with Tukey's multiple comparisons test. *** = $p < 0.001$, ns = not significant.

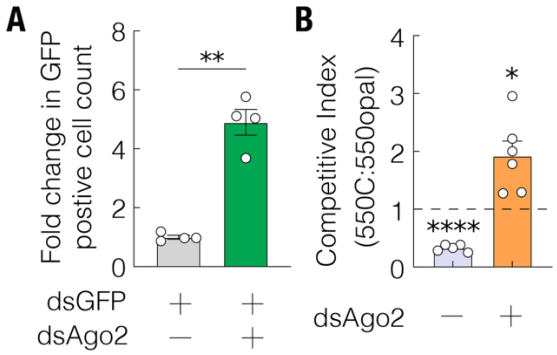

Fig. S5. Effect of *Ago2* KD on siRNA activity and SINV 550C competitive fitness in *Dcr2+* cells. (A) Effect of dsRNA-mediated *Ago2* silencing on GFP reporter expression in *Dcr2+* mosquito cells co-treated with *GFP* double-stranded RNA (dsGFP) as quantified by flow-cytometry. Error bars represent the standard error of the mean (SEM). Student's t-test. ** = $p < 0.01$. Two-way ANOVA with Tukey's multiple comparisons test. (B) Effect of dsAgo2 treatment on the replication of wild-type SINV 550opal and SINV 550C in *Dcr2+* mosquito cells as quantified by luciferase assay. The data is representative of two independent experiments. (B) Competitive fitness of SINV 550C variant against wild-type SINV 550opal in U4.4 cells treated with dsAgo2. The data represent five independent biological replicates. Error bars represent the standard error of the mean (SEM). One-sample t-test compared to a neutral competitive index (550C:550opal) of 1. **** = $p < 0.0001$, * = $p < 0.05$.

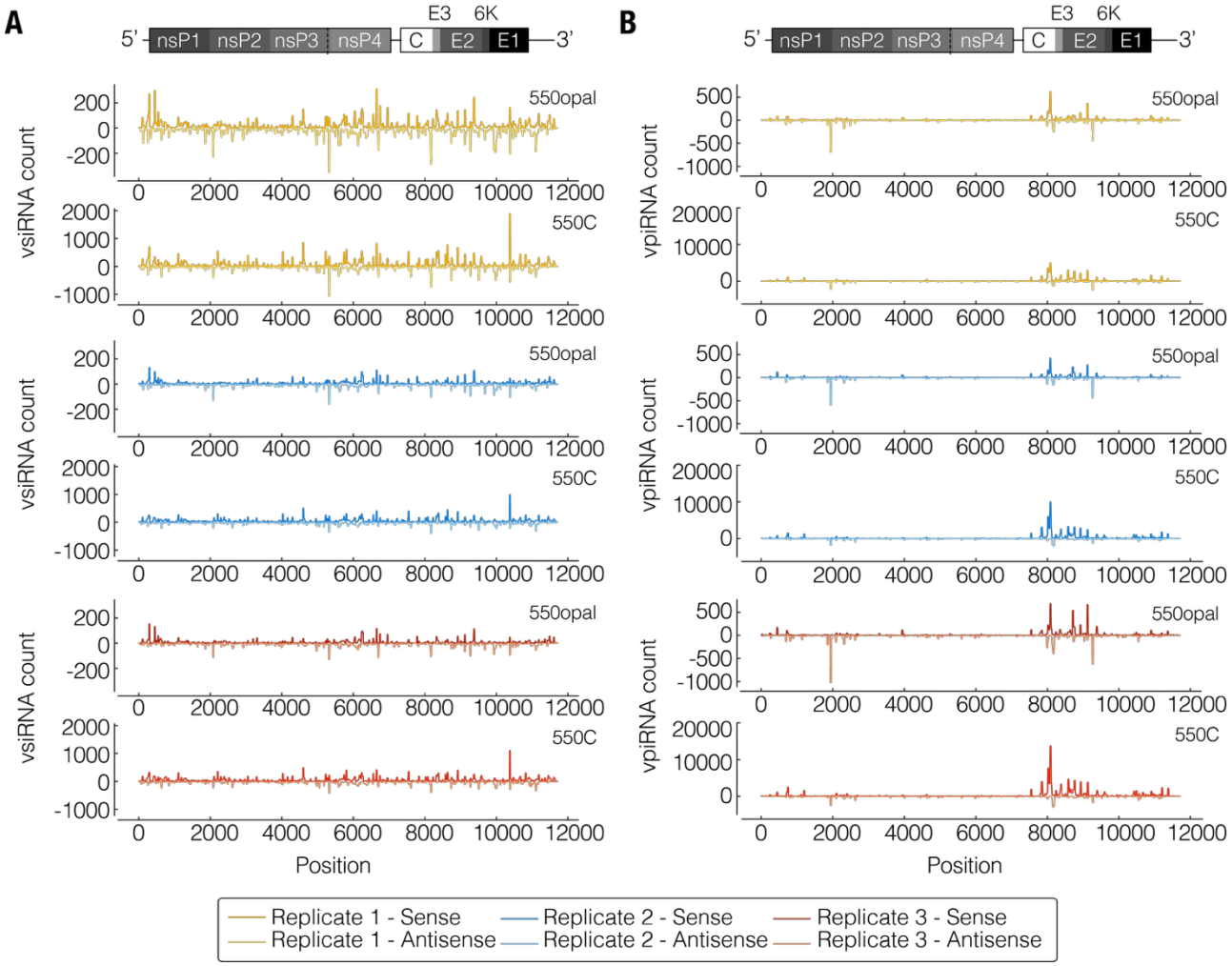

Fig. S6. Replicate data for virus-mapped vsiRNA and vpiRNAs in *Dcr2*+ mosquito cells. (A) Normalized vsiRNA read distribution in *Dcr2*+ cells infected with wild-type SINV 550opal and SINV 550C. (B) Normalized vpiRNA read distribution in *Dcr2*+ cells infected with wild-type SINV 550opal and SINV 550C.

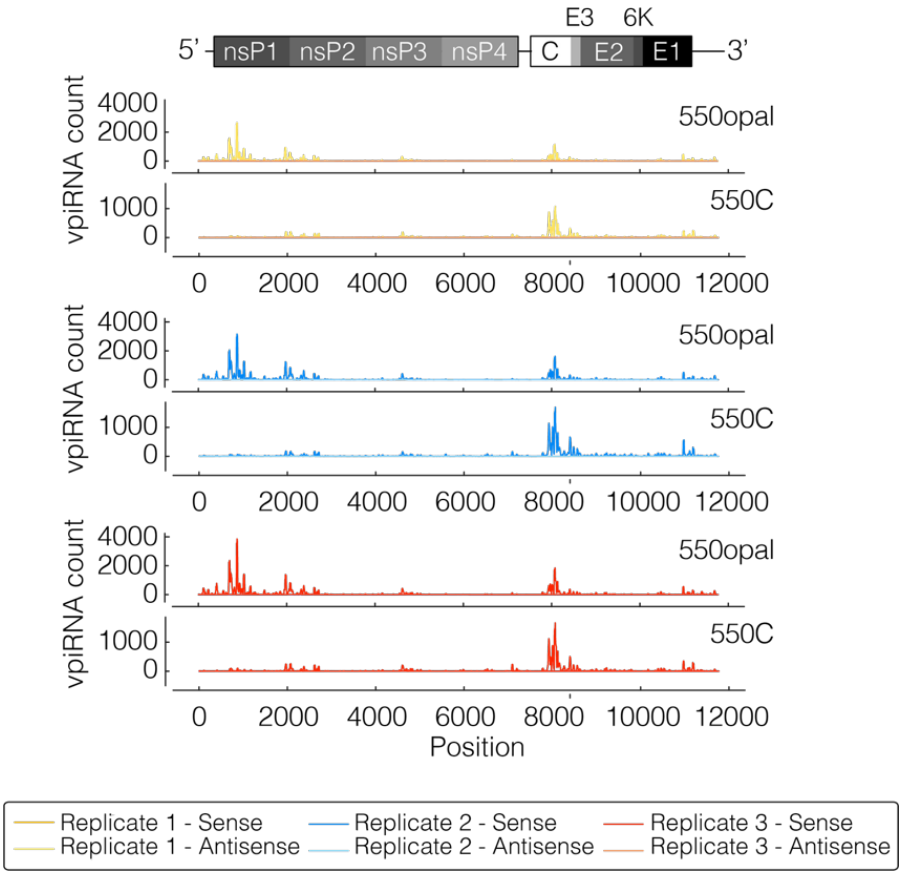

Fig. S7. Replicate data for virus-mapped vpiRNAs in *Dcr2*– mosquito cells. Normalized vpiRNA read distribution in *Dcr2*– cells infected with wild-type SINV 550opal and SINV 550C.

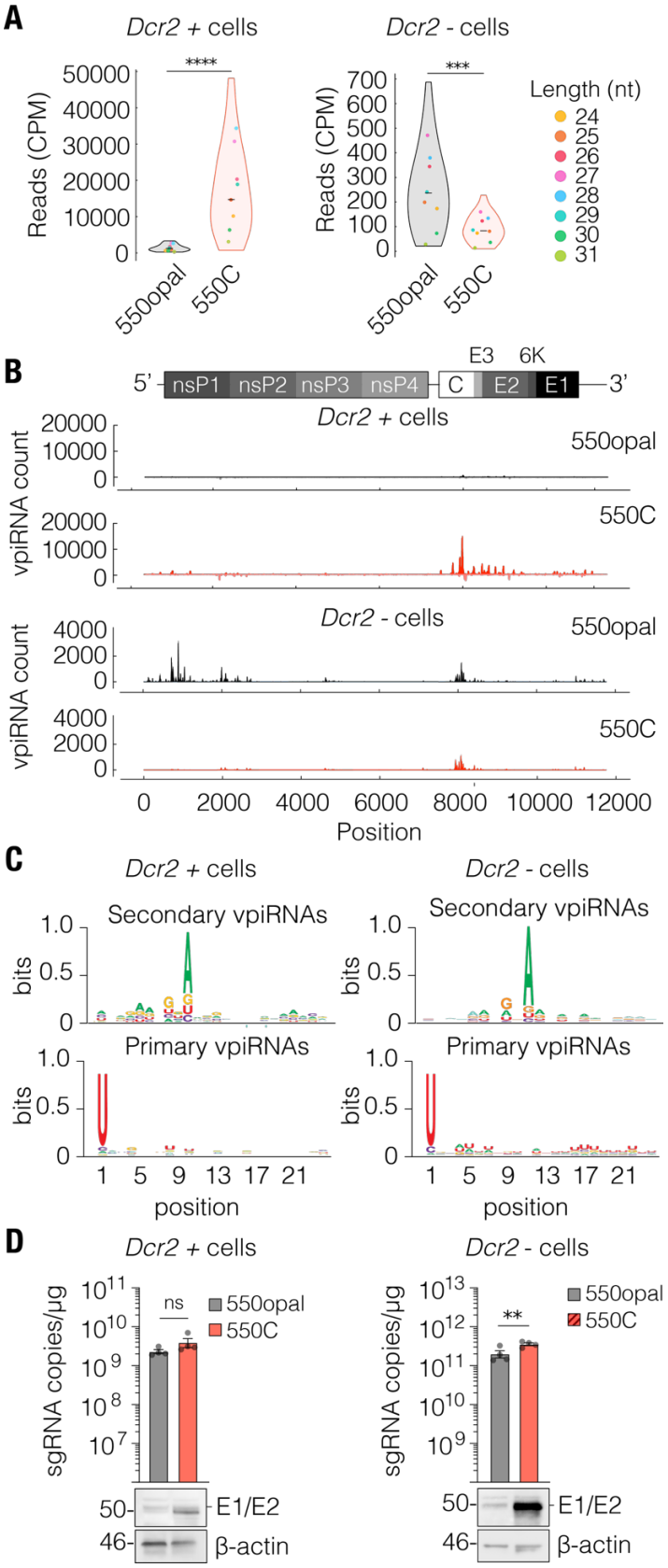
A
Dcr2 + cells
Dcr2 - cells
Reads (CPM)
****
***
550opal
550C
Length (nt)
24
25
26
27
28
29
30
31
B
5'
nsP1
nsP2
nsP3
nsP4
C
E3
6K
E2
E1
3'
vpiRNA count
Position
C
Secondary vpiRNAs
Primary vpiRNAs
bits
position
D
sgRNA copies/µg
ns
**
E1/E2
β-actin

Fig. S8. Virus-derived piRNAs are not antiviral in mosquito cells. (A) Normalized median read counts of vpiRNAs of different size classes in *Dcr2*+ U4.4 cells infected with wild-type SINV 550opal or SINV 550C viruses. Student's t-test. (B) Distribution of vpiRNA reads derived from wild-type SINV 550opal (in grey) or SINV 550C (in red) viruses in *Dcr2*+ U4.4 cells. Positive and negative Y-axis values represent read counts mapped to the sense and antisense strands at every position along the SINV genome and subgenome (X-axis). (C) Cumulative per-position nucleotide frequency of the first 24 bases in sense (Top) and antisense (Bottom) vpiRNA reads derived from *Dcr2*+ U4.4 cells infected with wild-type SINV 550opal or SINV 550C viruses. Logoplots were generated using WebLogo 3. (D) (Top) Levels of intracellular viral subgenomic RNA in *Dcr2*+ U4.4 cells infected with wild-type SINV 550opal or SINV 550C viruses as quantified via qRT-PCR. (Bottom) Western blot analysis of E1/E2 structural glycoprotein levels in *Dcr2*+ U4.4 cells infected with wild-type SINV 550opal or SINV 550C viruses. The data represent four independent biological replicates. Error bars represent the standard error of the mean (SEM). Student's t-test. **** = $p < 0.0001$, *** = $p < 0.001$, ** = $p < 0.01$, ns = not significant.

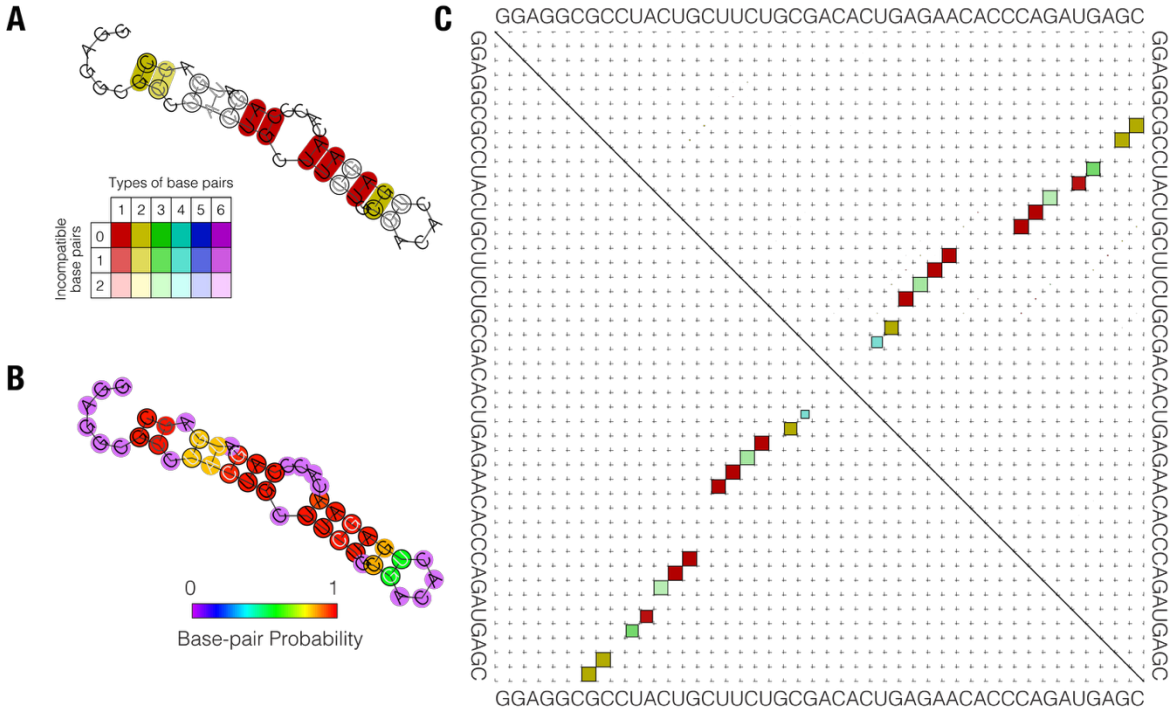

Fig. S9. Sequence and structural conservation of E1-hs RNA across alphaviruses. (A) RNAlifold predicted structure of the E1-hs region spanning SINV nucleotides 10328-10372. Colors highlight the mutational pattern with respect to the predicted RNA structure. The color key indicates whether a predicted base pair is formed by several different combinations of nucleotides, or whether consistent or compensatory mutations have occurred. Pale colors indicate the absence of base pairing in some sequences in the alignment. (B) Base-pairing probability of the predicted RNA structure. (C) Base-pairing probability matrix of the E1-hs region. The upper triangle shows pairing probabilities, with box size proportional to the likelihood of a base pair (i, j). The lower triangle depicts the minimum free energy (MFE) structure using uniformly sized boxes. In alignments, dot plots are color-coded to indicate sequence variation (refer to panel A). Note: Some weakly conserved base pairs are not displayed in panel A but are visible in panel C.

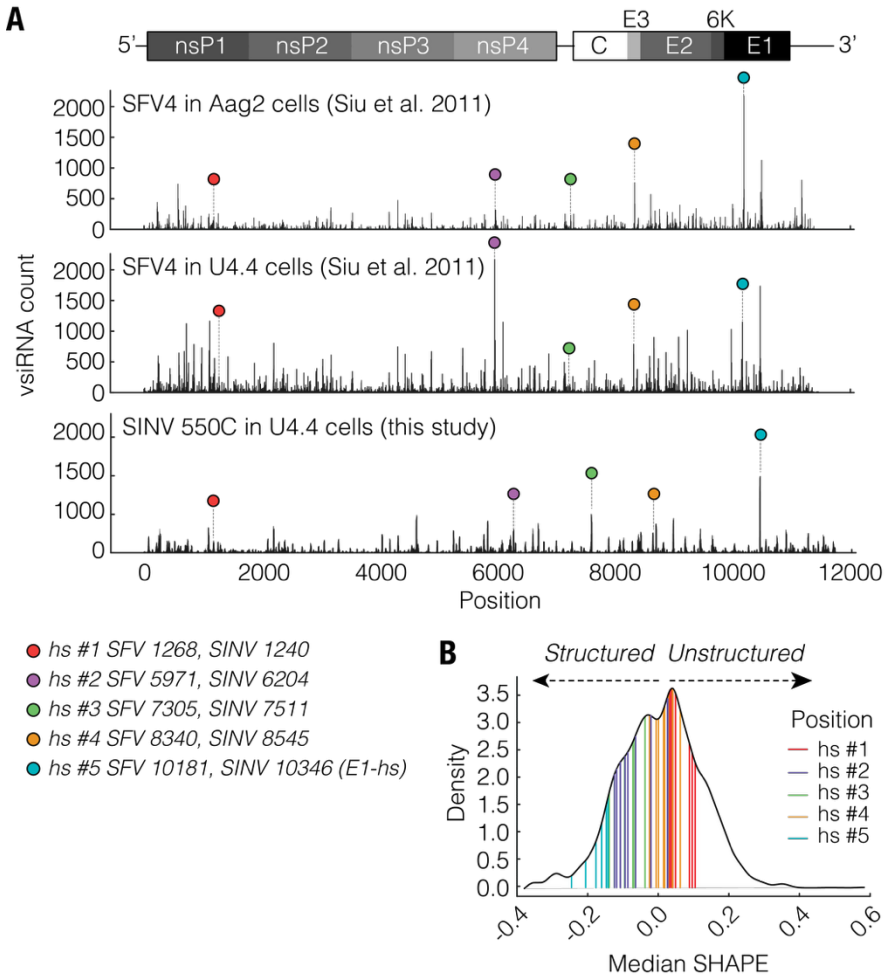

Fig. S10. Shared vsiRNA hotspots between distantly related alphaviruses. (A) vsiRNA hotspots identified within the Semliki Forest virus (SFV4) genome by *Siu et al.* in RNAi-competent *Aedes aegypti*-derived Aag2 (Top) and *Aedes albopictus*-derived U4.4 (Middle) cells. (Bottom) vsiRNA hotspots identified within SINV 550C in *Aedes albopictus*-derived U4.4 cells in this study. Four shared hotspots at SINV positions 1240, 7511, 8545, and 10346 are highlighted with colored circles (see key for details). (B) Density distribution profile of median SHAPE values of SINV RNA. Median SHAPE values for hotspot-region residues are highlighted in color.

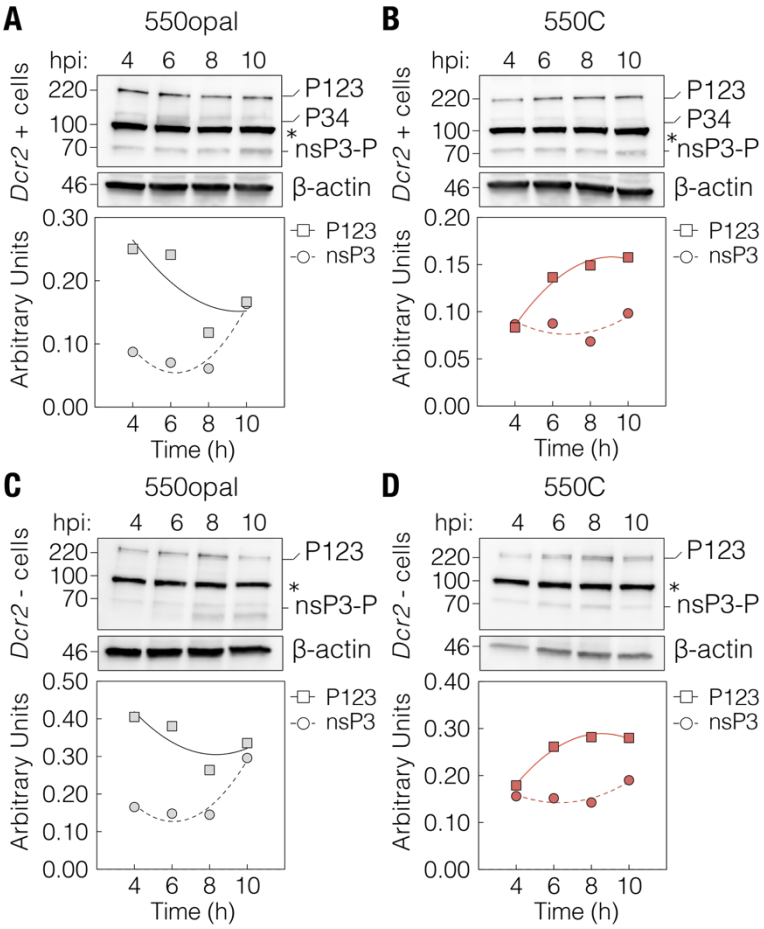

Fig. S11. Non-structural polyprotein processing cadence in mosquito cells. Temporal changes in the levels of unprocessed (P123) and processed (nsP3) nsP protein as determined by densitometric analysis of western blot data from (A-B) *Dcr2*+ (U4.4) and (C-D) *Dcr2*– (C6/36) cells infected with wild-type SINV 550opal (A, C) and SINV 550C (B, D). Harvested protein lysates were probed with anti-FLAG (nsP3) antibody. β-actin was used as a loading control. A non-specific band, cross-reactive with the anti-FLAG antibody, is denoted with an asterisk (*). The data is representative of two independent experiments.

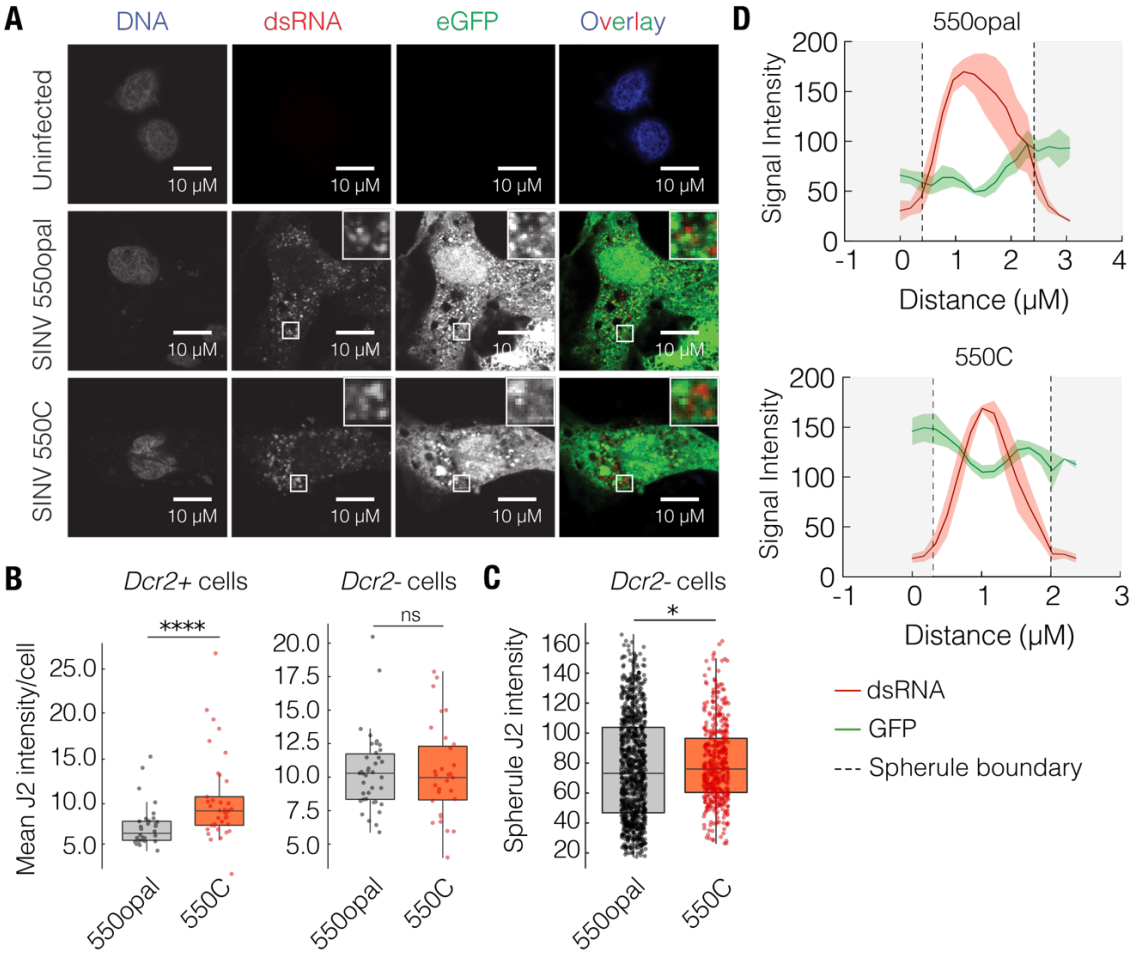

Fig. S12. J2 signal quantification in SINV-infected *Dcr2-* cells. (A) Localization of viral dsRNA (identified by the J2 antibody) and virally encoded GFP in *Dcr2-* C6/36 cells that were either uninfected or infected with wild-type SINV 550opal (top) or SINV 550C (bottom) as determined by confocal microscopy. The inset shows the localization of GFP and dsRNA around viral replication spherules. (B) Mean J2 intensity per cell in *Dcr2+* U4.4 (left) and *Dcr2-* C6/36 (right) cells infected with wild-type SINV 550opal and SINV 550C. (C) Spherule J2 intensity in *Dcr2-* C6/36 cells infected with wild-type SINV 550opal and SINV 550C. Error bars indicate the standard error of the mean (SEM). Mann-Whitney U-test.**** = $p < 0.0001$, * = $p < 0.05$, ns = not significant. (D) Two-dimensional (2D) plot profile of spherules in *Dcr2+* cells infected with wild-type and variant SINV. Dashed vertical lines indicate spherule boundaries.